

Efficient training-image based geostatistical simulation and inversion using a spatial generative adversarial neural network

Eric Laloy*, Romain Hérault†, Diederik Jacques‡ and Niklas Linde§

July 7, 2017

Abstract

Probabilistic inversion within a multiple-point statistics framework is still computationally prohibitive for large-scale problems. To partly address this, we introduce and evaluate a new training-image based simulation and inversion approach for complex geologic media. Our approach relies on a deep neural network of the spatial generative adversarial network (SGAN) type. After training using a training image (TI), our proposed SGAN can quickly generate 2D and 3D unconditional realizations. A key feature of our SGAN is that it defines a (very) low-dimensional parameterization, thereby allowing for efficient probabilistic (or deterministic) inversion using state-of-the-art Markov chain Monte Carlo (MCMC) methods. A series of 2D and 3D categorical TIs is first used to analyze the performance of our SGAN for unconditional simulation. The speed at which realizations are generated makes it especially useful for simulating over large grids and/or from a complex multi-categorical TI. Subsequently, synthetic inversion case studies involving 2D steady-state flow and 3D transient hydraulic tomography are used to illustrate the effectiveness of our proposed SGAN-based probabilistic inversion. For the 2D case, the inversion rapidly explores the posterior model distribution. For the 3D case, the inversion recovers model realizations that fit the data close to the target level and visually resemble the true model well. Future work will focus on the inclusion of direct conditioning data and application to continuous TIs.

1 Introduction

Capturing subsurface complexity and connectivity is of utmost importance for reliable groundwater modeling and uncertainty quantification (e.g., *Mariethoz and Caers, 2014; Linde et al., 2015*). Subsurface flow and transport modeling studies often rely on inversion methodologies to resolve subsurface structures that are consistent with both available prior information and indirect measurements of one or more state variables such as hydraulic head or concentration. When it is unrealistic to assume that the subsurface is multi-Gaussian (e.g., *Gómez-Hernández and Wen, 1998; Journel and Zhang, 2006*), one popular solution is to resort to multiple-point statistics (MPS) simulation (e.g., *Strebel, 2002; Mariethoz et al., 2010*). MPS techniques generate model realizations that honor a prior model which is defined by a training image (TI). The TI is a

*Belgian Nuclear Research Centre, Engineered and Geosystems Analysis. Email: elaloy@sckcen.be

†Normandie Univ, UNIROUEN, UNIHAVRE, INSA Rouen, LITIS, 76000 Rouen, France

‡Belgian Nuclear Research Centre, Engineered and Geosystems Analysis

§Applied and Environmental Geophysics Group, Institute of Earth Sciences, University of Lausanne

large gridded 2D or 3D unconditional representation of the expected target spatial field that can be either continuous or categorical (e.g., geologic facies image). Despite recent advances (e.g., Zahner *et al.*, 2016; Laloy *et al.*, 2016; Jäggli *et al.*, 2017), MPS-based probabilistic inversion is slow and the exploration of the posterior density is often incomplete. This has led to various model reduction techniques (e.g., Vo and Durlofsky, 2014, and references therein), which overall do not provide model realizations with a high degree of geological realism. The problem of how to address inversion in the presence of complex geological priors is, thus, a largely open and important research question. Although progresses are continuously made (e.g., Li *et al.*, 2016; Tahmasebi and Sahimi, 2016), even without considering inversion pure MPS simulation can also be prohibitively slow for large simulation grids and/or complex TIs.

Deep learning is currently transforming science and associated industries (Goodfellow *et al.*, 2016). Deep learning can be thought of as a class of mathematical models that learn a new parametric representation of the data that are given to them and, for some specific models, perform the inverse mapping from the learned representation to the original data space. Technically speaking, "deep" refers to the number of layers of a so-called (artificial) neural network. Yet it also more broadly relates to both model flexibility and complexity. A deep model is provided with raw (non-"handcrafted") data and constructs complex representations that are expressed in terms of other, simpler representations (e.g., Goodfellow *et al.*, 2016). Recently, Laloy *et al.* (Under Review) have proposed a deep neural network model of the variational autoencoder (VAE) type to build a low-dimensional parameterization of complex binary geologic prior models, and to perform probabilistic inversion within the resulting low-dimensional parameter space. This approach was shown to outperform state-of-the-art MPS-based inversion for the considered problems. Nevertheless, the approach by Laloy *et al.* (Under Review) suffers from three limitations: (1) it needs a large set (tens of thousands) of training images, (2) it is applicable to binary geologic models only and (3) it defines a global model compression in which each low-dimensional parameter influences the whole spatial model domain. In this work, we solve these three issues by using a totally different neural network called spatial generative adversarial neural network (SGAN).

Generative neural networks are deep networks that can be trained to stochastically generate data with similar properties as a training dataset (e.g., Goodfellow *et al.*, 2016). Note that the term "data" is here used in a wide sense, and can thus include images, text, etc. Among existing approaches, generative adversarial networks (GAN, Goodfellow *et al.*, 2014) have become increasingly popular in the field of deep learning. The main specificity of GANs is that they are learned by creating a competition between the actual generative model or "generator" and a discriminator in a zero-sum game framework (Goodfellow *et al.*, 2014). Both of these components are learned jointly. The discriminator tries to distinguish between real (training) data and generated data (i.e., to detect imperfections in the realizations), and the generator aims at fooling the discriminator, thereby, improving the realizations. A large variety of GANs have recently been proposed to generate different types of high-dimensional data, mostly images, (e.g., Radford *et al.*, 2016; Jethchev *et al.*, 2016), but also sound (e.g., Yang *et al.*, 2017) and text (e.g., Liang *et al.*, 2017) to list a few.

In this work, we introduce and evaluate the performance of a spatial GAN (SGAN) for fast training image-based unconditional geostatistical simulation and, more importantly, efficient inversion in 2D and 3D domains. We propose a 3D extension of the original 2D SGAN by Jethchev *et al.* (2016). For inversion, we take advantage of the fact that, similarly to the deep variational autoencoder (VAE) proposed by Laloy *et al.* (Under Review), the standard GAN architecture defines a low-dimensional "latent" rep-

representation of the original high-dimensional data (spatial subsurface property fields in our case). In such an architecture, the high-dimensional data (property fields in our case) realizations are obtained by propagating a low-dimensional random noise vector through the network. The inversion parameters can thus be defined, and the inversion can be performed, within this low-dimensional latent space. Our SGAN has the additional beneficial property that the latent space has a 2D or 3D spatial structure: each dimension of the low-dimensional space controls a well-defined fraction of the high-dimensional 2D or 3D spatial domain over which the geostatistical realizations are produced. Compared to our previous work with a VAE (*Laloy et al.*, Under Review), our SGAN has the following advantages: (1) training the network is performed using a single training image only, (2) it is fully 3D, (3) it can handle both binary and multi-categorical data (geological facies in our case) and, in principle, continuous data (e.g., hydraulic conductivity fields) as well, (4) it is designed such that each dimension of the latent space influences a specific part of the high-dimensional domain, and (5) it results into an even more compact representation of high-dimensional 3D domains with a dimensionality reduction that can exceed 4 orders of magnitude. Moreover, model generation with the 2D/3D SGAN proposed herein is very fast. For instance, a 3D model realization containing two millions of grid cells can be generated in less than 3 seconds on a standard desktop computer once the neural network has been learned. The main disadvantage of our proposed SGAN is that direct conditioning to point data is not straightforward and our emphasis is therefore on geostatistical simulation and inversion without direct conditioning. Some potential solutions to perform conditional simulation and/or include direct conditioning data within the inversion are briefly discussed.

The geostatistical simulation component of our paper has similarities with the independently developed study by *Mosser et al.* (2017), where a slightly different type of GAN called DCGAN (e.g., *Radford et al.*, 2016) is used for 3D generation of binary porous systems. The main differences between our work and that of Mosser and coworkers are as follows. First, for our SGAN each dimension of the low-dimensional latent representation influences only a given region of the original model domain, which is beneficial for inversion. Second, we consider more complex training images than the binary images investigated by *Mosser et al.* (2017). Indeed, our used TIs show a much larger degree of connectivity and can be multi-categorical. Finally and most important, we use our proposed SGAN to perform geostatistical inversion.

This paper is organized as follows. Section 2 presents the different elements needed for (unconditional) geostatistical simulation and inversion. This is followed in section 3 with a performance analysis of the geostatistical simulation using several 2D and 3D categorical TIs. Synthetic 2D and 3D experiments involving both steady-state and transient groundwater flow are then used in section 4 to demonstrate the inversion capabilities. In section 5, we discuss the advantages and limitations of our proposed method and outline possible future developments. Finally, section 6 concludes with a summary of the most important findings.

2 Methods

2.1 Spatial Generative Adversarial Network Architecture

Our proposed network is a 3D extension of the 2D SGAN by *Jetchev et al.* (2016). This neural network is a type of deep neural network (DNN) that is built of direct and transposed convolutional layers only. Basically, neural networks approximate the (potentially complex) relationships between input, \mathbf{x} , and output, \mathbf{y} , data vectors by

combining many computational units called “neurons”. In addition, the classical DNN architecture stacks successive layers of neurons. A typical formulation of the neuron is given by

$$h(\mathbf{x}) = f(\langle \mathbf{x}, \mathbf{w} \rangle + b), \quad (1)$$

where $h(\cdot)$ signifies the scalar output of the neuron, $f(\cdot)$ is a nonlinear function that is called the “activation function”, $\langle \cdot, \cdot \rangle$ denotes the scalar product, $\mathbf{w} = [w_1, \dots, w_N]$ is a set of weights of the same dimension, N , as \mathbf{x} and b represents the bias associated with the neuron. To be useful, a DNN must be trained or “learned”. In the learning process the values in \mathbf{w} and b are optimized for each neuron such that the DNN performs a prespecified task as well as possible. When $f(\cdot)$ is differentiable, \mathbf{w} and b can be optimized by gradient descent. Typical forms of $f(\cdot)$ include the rectified linear unit (ReLU), sigmoid function and hyperbolic tangent function (e.g., *Goodfellow et al.*, 2016).

The convolutional layer forms the fundamental building block of the convolutional neural network (CNN) type of architecture. The convolutional operator has gained widespread use for image processing because it explicitly considers the spatial structure in the input data. When the input is a 2D image (with possibly 3 channels for a RGB image), a convolutional layer, \mathbf{h} , is constructed by means of a series of $k = 1, \dots, N_k$ small $N_i \times N_j$ filters, \mathbf{w}^k , that convolve an input pixel, $X_{u,v}$ to $h_{u,v}^k$ as

$$h_{u,v}^k(X_{u,v}) = f\left(\sum_{i=1, j=1}^{N_i, N_j} w_{i,j}^k X_{u+i, v+j} + b_k\right), \quad (2)$$

where a common choice for $f(\cdot)$ is the rectified linear unit (ReLU): $f(x) = \max(0, x)$. The resulting series of N_k \mathbf{h}^k stacked “feature maps” forms the convolutional layer \mathbf{h} . Note that the neuron defined by equation (2) is connected to only a local region of the input image (or volume for the 3D formulation). This enforces encoding of spatially-local information at the level of one convolutional layer. Therefore, the larger the number of stacked feature maps, N_k , the richer the representation of the input data. There are other important convolution parameters that, for brevity, we do not discuss in this paper. These are the “stride” parameter which controls the overlapping between successive moves in the forward pass of a given filter, the “padding” parameter that defines padding of the borders of the input images or volumes for size preservation, and the “pooling” parameter which involves non-linear down-sampling to reduce the size of a convolutional layer and thereby prevent overfitting. For further information on CNN layers, we refer the reader to *Goodfellow et al.* (2016) and online tutorials¹.

Figure 1 depicts the main SGAN architecture for the generation of 2D grayscale images. The 3D case obeys the same principles but it cannot easily be represented. The low-dimensional input or latent space, \mathbf{Z} , has a spatial structure and follows a bounded uniform distribution, $\mathbf{Z} \sim U(-1, 1)$. In the 2D case, \mathbf{Z} is a 3D array of size $m \times n \times q$. Each $Z_{(i,j,\cdot)}$ with $i = 1, \dots, m; j = 1, \dots, n$ controls a specific region of the generated full scale $w \times h$ image, \mathbf{X} . In addition, these specific regions partially overlap. This is illustrated for the $1 \times 1 \times q$ white-colored component of \mathbf{Z} in Figure 1. The third dimension, q , is not related to a spatial location but allows for additional flexibility in the data representation encoded by each q -dimensional element $Z_{(i,j,k=1\dots q)}$. For 3D grayscale image generation, $\mathbf{Z} \sim U(-1, 1)$ becomes a 4D array of size $m \times n \times o \times q$ where the dimensions m , n and o now correspond to specific regions of the generated

¹For instance: <http://deeplearning.net/tutorial/> and <http://cs231n.github.io/convolutional-networks/>.

full scale volume of size $w \times h \times l$. At generation time, the sampled \mathbf{Z} array enters the generator, $G(\mathbf{Z})$ to produce a (2D or 3D) grayscale image, \mathbf{X} (Figure 1). $G(\mathbf{Z})$ is made from a stack of transposed 2D or 3D convolutional layers (see *Dumoulin and Visin, 2016*, for details on the transpose operation for convolutional layers). At discrimination time, that is, during training either the generated image or a true image formed by a fraction of the TI (interchangeably called \mathbf{X} for now), is processed through the discriminator, $D(\mathbf{X})$, to output a $m \times n$ (2D case) or $m \times n \times o$ (3D case) field of probabilities for fake/real images (see also section 2.2).

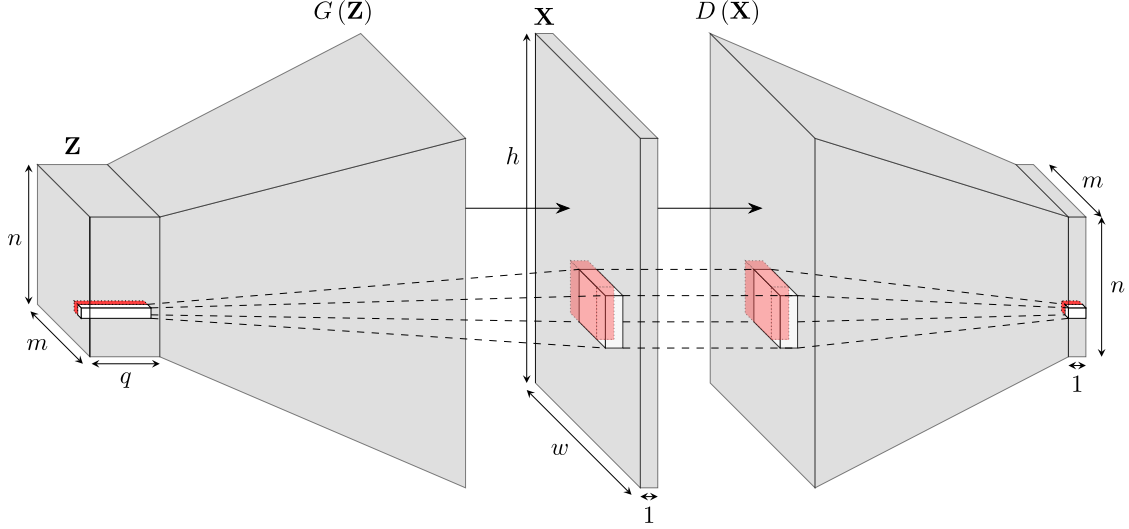


Figure 1: Illustration of the SGAN structure for the 2D case. A input $m \times n \times q$ \mathbf{Z} array of uniform variables $\sim U(-1, 1)$ is propagated through the generator, $G(\mathbf{Z})$, to produce a grayscale image, \mathbf{X} . During learning, the generated \mathbf{X} and true \mathbf{X} iteratively enter the discriminator, $D(\mathbf{X})$. The latter produces a $m \times n$ array of probabilities, the mean of which is taken as the probability that the incoming \mathbf{X} belongs to the TI. Generator and discriminator are made of stacked transposed and non-transposed convolutional layers, respectively. The network structure for the 3D case obeys the same logic but it cannot easily be represented.

The computational cost incurred by training a deep generative model largely depends on the size of the model realization domain. Due to their purely convolutional nature, the original 2D SGAN and our 3D extension can be trained at low computational cost using a relatively small realization domain, and then be subsequently used to generate arbitrarily large realizations that match the spatial statistics found in the training data. For a square ($w \times h$) or cubic ($w \times h \times l$) generation domain, the relationship between $z_x = m = n = o$ and $x_x = w = h = l$ is given by

$$x_x = [z_x - 1] 2^{dp} + 1, \quad (3)$$

where dp is the number of stacked convolutional layers in $G(\mathbf{Z})$. This allows for a rather strong dimensionality reduction of the TI space. We refer to *Jetchev et al. (2016)* for more details on the (2D) SGAN architecture.

For all our experiments, we used squared or cubic filters with side length (N_i in equation (2)) in the range 3-9 depending on the case study and the same activation functions ($f(\cdot)$ in equation (2)) as in *Jetchev et al. (2016)*. These are: ReLU (all but last layer) and hypertangent (last layer) for $G(\mathbf{Z})$ and so-called "leaky" ReLU (all but last layer) and sigmoid (last layer) for $D(\mathbf{X})$. Moreover, we always considered a stack

of $dp = 5$ convolutional layers for both $G(\mathbf{Z})$ and $D(\mathbf{X})$ with the following number of feature maps (N_k in equation (2)) from \mathbf{Z} to \mathbf{X} : [512, 256, 128, 64, 1].

Using $dp = 5$ together with $q = 1$, as we do for 2 out of our 4 test cases, equation (3) predicts that 3D realizations of size $129 \times 129 \times 129$ can be generated by drawing as few as $5 \times 5 \times 5 = 125$ Z variables from the $U(-1, 1)$ distribution. This corresponds to a more than 4 orders of magnitude dimensionality reduction. Note that in this study, we never used a q value larger than 3. For the above example, $q = 3$ would still lead to a more than 3 orders of magnitude dimensionality reduction.

Similarly as the original 2D SGAN, our 3D extension was implemented within the open-source LASAGNE Python software (*Dieleman et al.*, 2016) which works on top of the open-source THEANO Python library (*Theano*, 2016).

2.2 Training The Generative Adversarial Network

The specificity of the GAN architecture is that the generator and discriminator are trained (or "learned") simultaneously with opposed goals. The discriminator, $D(\mathbf{X})$, is fed with samples from the "real" training set, which from now on will be referred to as \mathbf{X} with distribution $p_{\text{data}}(\mathbf{X})$, and "fake" samples (i.e., realizations) created by the generator: $\hat{\mathbf{X}} = G(\mathbf{Z})$. The real samples \mathbf{X} are a set of patches randomly cut from the TI. The discriminator tries to distinguish between \mathbf{X} and $\hat{\mathbf{X}}$ by computing for each received sample the probability that it belongs to $p_{\text{data}}(\mathbf{X})$. In contrast, the generator, $G(\mathbf{Z})$ aims at fooling $D(\cdot)$ into labeling $\hat{\mathbf{X}}$ as a sample from $p_{\text{data}}(\mathbf{X})$ and thus achieving a mean $D(\hat{\mathbf{X}}) = D(G(\mathbf{Z}))$ close to 1 (*Goodfellow et al.*, 2014). Mathematically, this translates into the following minimization-maximization loss function

$$\min_{G(\cdot)} \max_{D(\cdot)} \{ \mathbb{E}_{\mathbf{X} \sim p_{\text{data}}(\mathbf{X})} [\log(D(\mathbf{X}))] + \mathbb{E}_{\mathbf{Z} \sim p_{\mathbf{Z}}(\mathbf{Z})} [\log(1 - G(\mathbf{Z}))] \}. \quad (4)$$

In practice, the minimization-maximization problem in equation (4) is solved in two consecutive steps. First one minimizes

$$\mathcal{L}^D = -\mathbb{E}_{\mathbf{X} \sim p_{\text{data}}(\mathbf{X})} [\log(D(\mathbf{X}))] - \mathbb{E}_{\mathbf{Z} \sim p_{\mathbf{Z}}(\mathbf{Z})} [\log(1 - G(\mathbf{Z}))] \quad (5)$$

while keeping the parameters of $G(\mathbf{Z})$ (that is, the \mathbf{W} and \mathbf{b} of each layer of $G(\mathbf{Z})$) fixed to current values. Second, one minimizes

$$\mathcal{L}^G = -\mathbb{E}_{\mathbf{Z} \sim p_{\mathbf{Z}}(\mathbf{Z})} [\log(1 - G(\mathbf{Z}))] \quad (6)$$

with the parameters of $D(\cdot)$ fixed to current values.

For numerical stability, least-squares regularization operators for both the generator and discriminator weights are added to equations (5) and (6). Approximating the expectations by sums and using the parameterization trick by *Goodfellow et al.* (2014), this leads (for the 3D case) to the following formulations

$$\mathcal{L}^D = -\frac{1}{mno} \sum_{i=1}^m \sum_{j=1}^n \sum_{k=1}^o \log(1 - D_{ijk}(G(\mathbf{Z}))) - \frac{1}{mno} \sum_{i=1}^m \sum_{j=1}^n \sum_{k=1}^o \log(D_{ijk}(\mathbf{X})) + \alpha \|\mathbf{\Omega}_D\|_2 \quad (7)$$

and

$$\mathcal{L}^G = -\frac{1}{mno} \sum_{i=1}^m \sum_{j=1}^n \sum_{k=1}^o \log(D_{ijk}(G(\mathbf{Z}))) + \alpha \|\mathbf{\Omega}_G\|_2 \quad (8)$$

where $\mathbf{\Omega}_D$ and $\mathbf{\Omega}_G$ contain the discriminator and generator weights, respectively, and α is a weight parameter that we set to 1×10^{-5} .

Since both $G(\mathbf{Z})$ and $D(\cdot)$ are differentiable, equations (7-8) can be minimized by stochastic gradient descent (that is, gradient descent using a series of mini-batches rather than all the data at once) together with back propagation. This means that the loss function derivative is propagated backwards throughout the network using the chain rule, in order to update the parameters. Various stochastic gradient descent algorithms are available. In this work, we used the adaptive moment estimation (ADAM) algorithm which has been proven efficient for different types of deep networks (*Kingma and Ba, 2015*).

The minimization of equations (7-8) was performed on a GPU Tesla K40 and training the SGAN for 50 epochs (full cycles of the stochastic gradient descent) took between 3 and 12 hours, depending mostly on the size of the model domain used for learning (from 129×129 to $97 \times 97 \times 97$) and the chosen number of patches in a training batch (from 25 to 64 depending on GPU memory availability).

Training of GANs is notoriously unstable, in the sense that image generation quality may not necessarily increase as training progresses (e.g., *Salimans et al., 2016*; *Sønderby et al., 2016*; *Mosser et al., 2017*). To mitigate this unstable behavior, we followed *Sønderby et al. (2016)* and added a Gaussian white noise with standard deviation of 0.1 to the input layer of $D(\cdot)$. Notwithstanding, this did not totally remove training instability. The final "best" network was therefore chosen a posteriori for each case study by visual and quantitative (see section 2.3) inspection of generation performance among the 50 trained networks associated with the achieved 50 training epochs. This final, manual model selection step is arguably tedious yet inherent to the current GAN state-of-the-art.

2.3 Generation Quality Assessment

Although our main goal is inversion, it is essential to verify that the unconditional realizations produced by our approach are consistent with the TI. To complement visual inspection of randomly chosen realizations, a series of quantitative metrics were used to evaluate generation performance. For each case study, the following structural indicators were computed for (1) the TI and (2) a set 100 (2D cases) or 25 (3D cases) random realizations obtained by our SGAN:

1. Two-point probability function (PF, *Torquato and Stell, 1982*),
2. Two-point cluster function (CF, *Torquato et al., 1988*) which is also called connectivity function (*Pardo-Igúzquiza and Dowd, 2003*),
3. Fractions of the different facies.

We refer the reader to the cited references for mathematical descriptions of these indicators. In short, the PF is the probability that 2 points separated by a given lag distance belong to the same facies while the CF is the probability that there exists a continuous path of the same facies between 2 points of the same facies separated by a given lag distance. Using the routines developed by *Lemmens et al. (2017)*, the PF, and CF were calculated for each facies along the x , y , and main diagonal, d_{xy} , directions for the 2D case studies. For the 3D case studies, the z and main diagonal d_{xz} and d_{yz} directions were additionally considered, leading to a total of 6 metrics for each combination of indicator and facies.

2.4 Bayesian inversion

A common representation of the forward problem is

$$\mathbf{d} = F(\boldsymbol{\theta}) + \mathbf{e}, \quad (9)$$

where $\mathbf{d} = (d_1, \dots, d_N) \in \mathbb{R}^N$, $N \geq 1$ is the measurement data, $F(\boldsymbol{\theta})$ is a deterministic forward model with parameters $\boldsymbol{\theta}$ and the noise term \mathbf{e} lumps all sources of errors.

In the Bayesian paradigm, parameters in $\boldsymbol{\theta}$ are viewed as random variables with a posterior pdf, $p(\boldsymbol{\theta}|\mathbf{d})$, given by

$$p(\boldsymbol{\theta}|\mathbf{d}) = \frac{p(\boldsymbol{\theta})p(\mathbf{d}|\boldsymbol{\theta})}{p(\mathbf{d})} \propto p(\boldsymbol{\theta})L(\boldsymbol{\theta}|\mathbf{d}), \quad (10)$$

where $L(\boldsymbol{\theta}|\mathbf{d}) \equiv p(\mathbf{d}|\boldsymbol{\theta})$ signifies the likelihood function of $\boldsymbol{\theta}$. The normalization factor $p(\mathbf{d}) = \int p(\boldsymbol{\theta})p(\mathbf{d}|\boldsymbol{\theta})d\boldsymbol{\theta}$ is not required for parameter inference when the parameter dimensionality is fixed. In the remainder of this paper, we will thus focus on the unnormalized density $p(\boldsymbol{\theta}|\mathbf{d}) \propto p(\boldsymbol{\theta})L(\boldsymbol{\theta}|\mathbf{d})$.

To avoid numerical over- or underflow, it is convenient to work with the logarithm of $L(\boldsymbol{\theta}|\mathbf{d})$ (log-likelihood): $\ell(\boldsymbol{\theta}|\mathbf{d})$. If we assume \mathbf{e} to be normally distributed, uncorrelated and with known constant variance, σ_e^2 , $\ell(\boldsymbol{\theta}|\mathbf{d})$ can be written as

$$\ell(\boldsymbol{\theta}|\mathbf{d}) = -\frac{N}{2} \log(2\pi) - N \log(\sigma_e) - \frac{1}{2} \sigma_e^{-2} \sum_{i=1}^N [d_i - F_i(\boldsymbol{\theta})]^2, \quad (11)$$

where the $F_i(\boldsymbol{\theta})$ are the simulated responses that are compared the $i = 1, \dots, N$ measurement data, d_i .

As no analytical solution of $p(\boldsymbol{\theta}|\mathbf{d})$ is available for the type of non-linear inverse problems considered herein, we sample from $p(\boldsymbol{\theta}|\mathbf{d})$ by MCMC simulation (see, e.g., *Robert and Casella*, 2004) with the DREAM_(ZS) algorithm (*Vrugt et al.*, 2009; *Laloy and Vrugt*, 2012). Various studies in hydrology and geophysics (amongst others) have shown that DREAM_(ZS) can derive posterior distributions with 25-250 dimensions (e.g., *Laloy et al.*, 2012, 2013; *Linde and Vrugt*, 2013; *Laloy et al.*, 2015; *Lochbühler et al.*, 2015). Since in this work the inversion is performed within the low-dimensional space defined by \mathbf{Z} , we have $\boldsymbol{\theta} = \mathbf{Z}$. Furthermore, we slightly modified the original DREAM_(ZS) algorithm by including a (vanishing) tempering of the likelihood function (by inflating the variance term in the likelihood function). Limited to the so-called burn-in (see, e.g., *Robert and Casella*, 2004), this tempering proved to be very useful for solving the inverse problems considered herein.

3 Geostatistical Simulation Results

As stated earlier, inversion is our primary objective. However, evaluating the quality of the geostatistical realizations produced by our approach is important as it will condition the ultimate quality of our inversion results.

3.1 2D Models

Our first 2D test case considers the 2500×2500 binary channelized TI depicted in Figure 2a. This TI is a hand-made drawing inspired by Strebel's TI (*Strebel*, 2002) by *Zahner et al.* (2016). For learning, we used $z_x = 12$ and $q = 1$. Consistently with setting $z_x = 12$ in equation (3), the training batch for each epoch was constructed by randomly cutting

64 patches of dimensions 353×353 from the TI. To generate realizations we set $z_x = 20$ and $q = 1$, thereby leading to a 400-dimensional \mathbf{Z} and realizations of size 609×609 . The learned SGAN model deemed to work best was achieved at training epoch 25 while networks learned after epochs 25-30 started to degrade (not shown). Moreover, the produced continuous model realizations (in $[0, 1]$) were processed through a median filter with kernel size of $(3, 3)$ before being thresholded at the 0.5 level.

Figure 3 presents 8 randomly chosen realizations, together with a 609×609 fraction of the TI. Visually, the realizations appear consistent with the TI. Figures 4 and 5 show the associated PF and CF metrics. Although some deviations exist, there is a generally good match between the realizations and the TI statistics. Also, the different realizations are slightly less variable than the TI's patches. It is important to note, however, that the ratio of the used size of a TI's patch to the size of the TI is about $1/17$. As opposed to the 100 SGAN-based realizations and associated metrics, the 100 TI's patches and associated metrics are therefore not independent. With respect to facies fractions, the TI has a matrix pixel proportion of 0.74 while the corresponding average over the 100 realizations is 0.73.

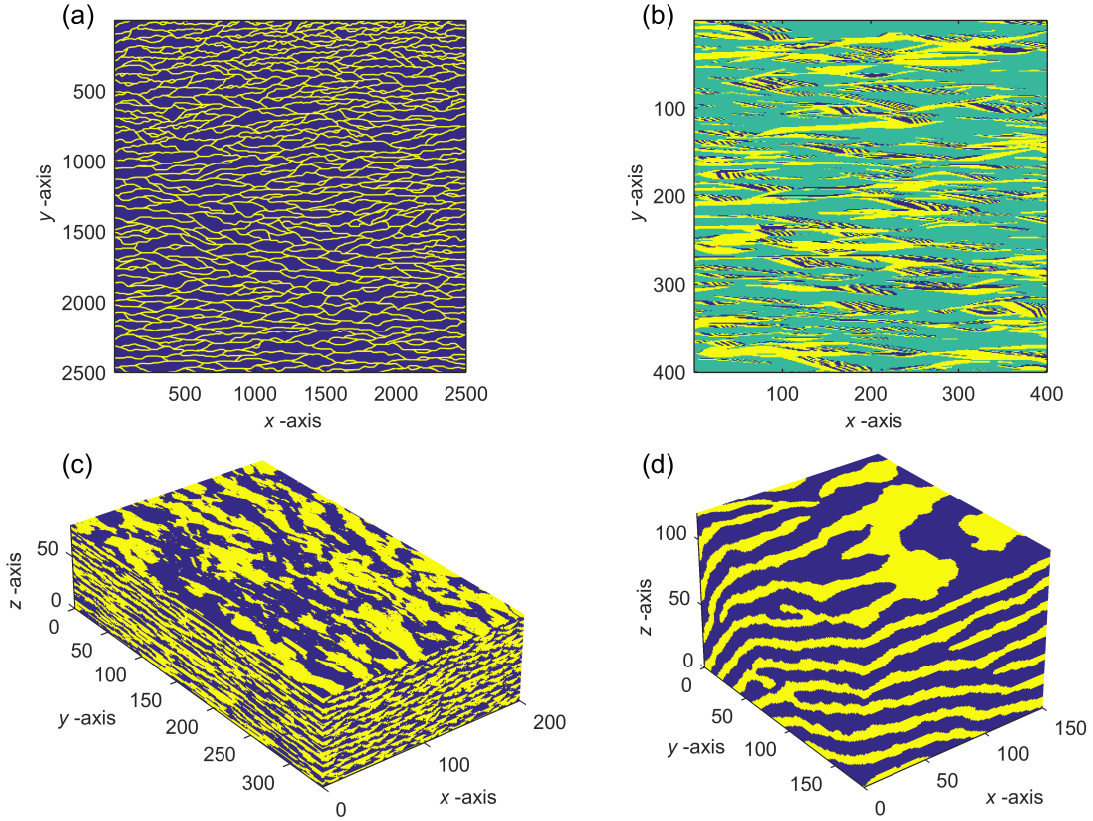


Figure 2: Four training images (TIs) used for the considered geostatistical simulation tests. The TIs are (a) the 2500×2500 hand-made drawing inspired by Strebelle's TI by *Zahner et al.* (2016), (b) the 400×400 braided river aquifer by *Pirot et al.* (2015), (c) the $340 \times 200 \times 80$ Maules Creek aquifer (available at <http://www.trainingimages.org/training-images-library.html>) and (d) the $180 \times 150 \times 120$ categorical fold aquifer from <http://www.trainingimages.org/training-images-library.html>. The 2D and 3D inverse case studies rely on the TIs depicted in (a) and (d), respectively.

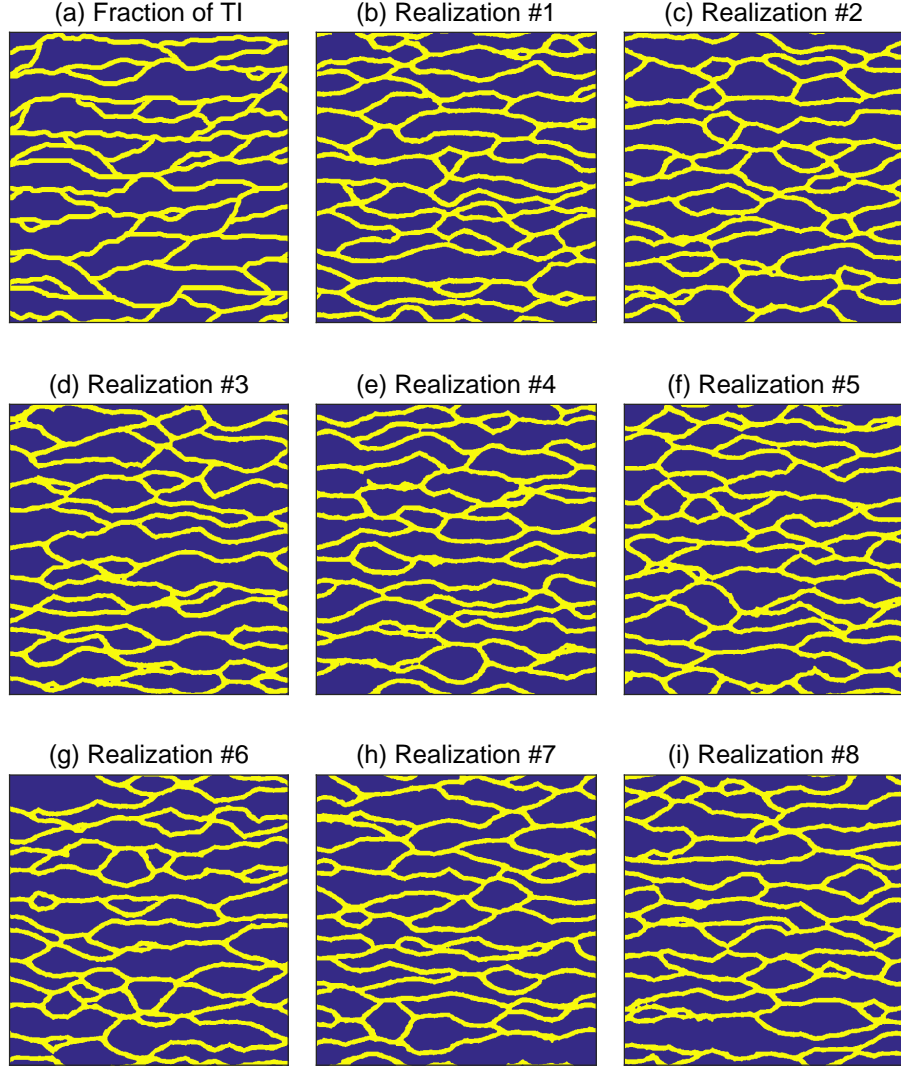


Figure 3: (a) Fraction of size 609×609 of the TI shown in Figure 2a and (b) - (i) randomly chosen 609×609 realizations derived by our SGAN. Each realization is generated by sampling 400 random numbers from a uniform distribution, $U(-1, 1)$.

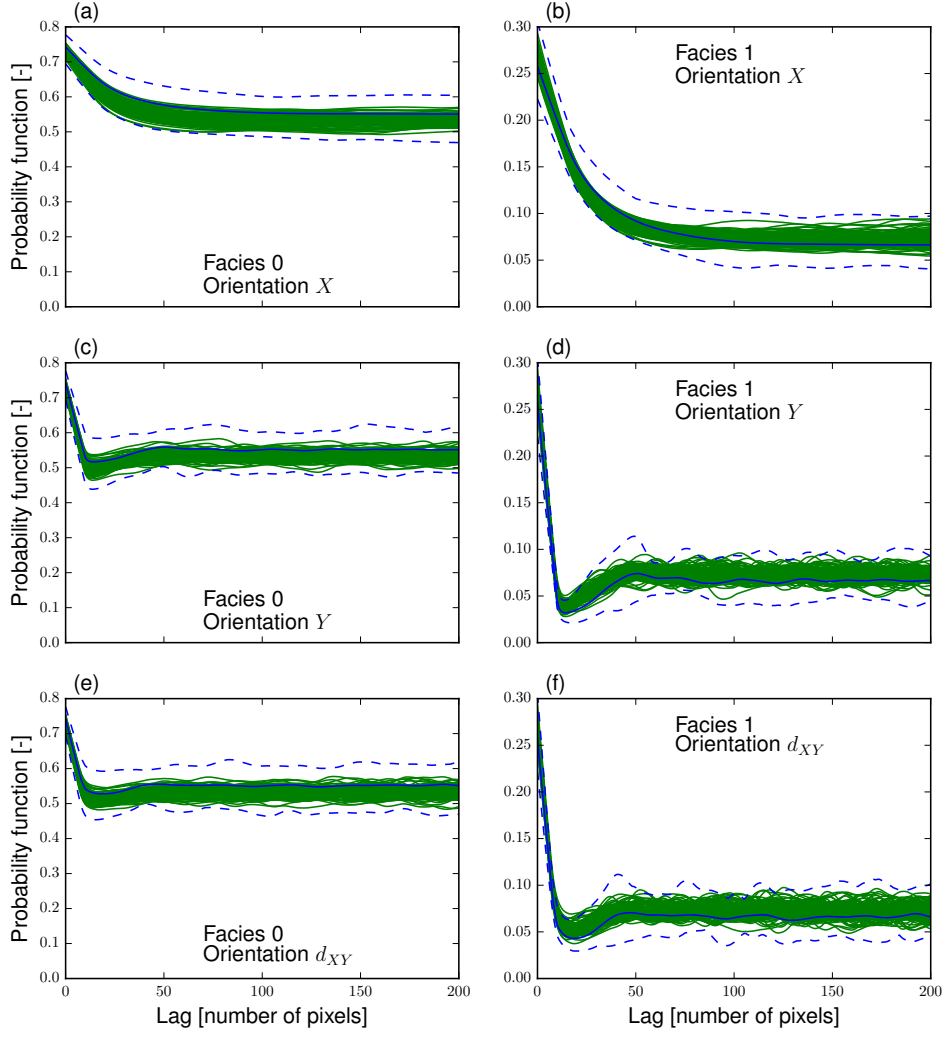


Figure 4: Probability function (PF) for the 2D case study involving the binary channelized aquifer TI depicted in Figure 2a. The blue lines refer to 100 randomly selected patches of size 609×609 from the 2500×2500 TI with the solid blue line indicating the mean and the 2 dashed lines representing the minimum and maximum values at each lag. The green solid lines represent 100 SGAN realizations of size 609×609 . The PF is calculated for each facies along spatial directions. The x and y symbols signify the x and y axes, and d_{xy} represents the diagonal direction formed by the 45° angle between the x and y axes.

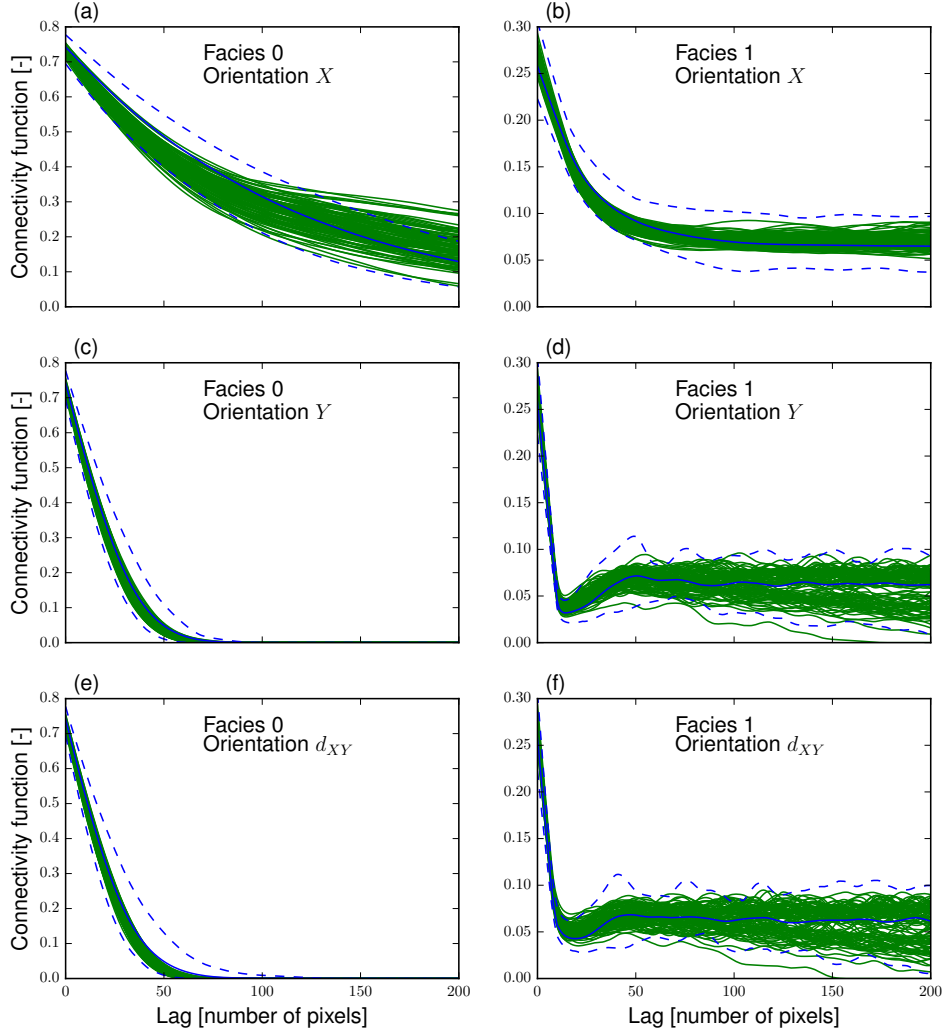


Figure 5: Cluster or connectivity function (CF) for the 2D case study involving the binary channelized aquifer TI depicted in Figure 2a. The blue lines refer to 100 randomly selected patches of size 609×609 from the 2500×2500 TI with the solid blue line indicating the mean and the 2 dashed lines representing the minimum and maximum values at each lag. The green solid lines represent 100 SGAN realizations of size 609×609 . The CF is calculated for each facies along spatial directions. The x and y symbols signify the x and y axes, and d_{xy} represents the diagonal direction formed by the 45° angle between the x and y axes.

Our second 2D case study involves the 400×400 tri-categorical TI shown in Figure 2b. This TI represents a braided river aquifer (*Pirot et al., 2015*). After some trial and error testing, here we used $z_x = 5$ and $q = 3$ for learning and $z_x = 10$ and $q = 3$ to generate the realizations. The size of the 64 training patches belonging to each epoch was thus 129×129 , while a 300-dimensional \mathbf{Z} was used to produce the analyzed 289×289 realizations. For this case study only, the number of training epochs was raised from 50

to 100 because image generation quality kept improving after epoch 50. The optimally-trained network model was judged to be that produced at epoch 92. The generated realizations were not filtered but thresholded as $\leq 0.33 = \text{facies } 0$, $0.33 < \dots \leq 0.67 = \text{facies } 1$ and $> 0.67 = \text{facies } 2$.

Figure 6 depicts 8 randomly chosen realizations, together with a 289×289 fraction of the TI. The realizations look fairly similar to the TI. Figures 7 and 8 show the associated PF and CF metrics. A relatively good correspondence between the TI and the realizations is observed. The main discrepancies are a larger spread in the realizations' statistics and the regular occurrence of small peaks in the PF of facies 1 and, to a lesser extent, for facies 2 (Figure 7). The larger spread in the SGAN-based realizations is however not surprising given that the TI's patches are strongly dependent for this example. Indeed, the ratio of the size of a TI's patch to the size of the TI is as large as (approximately) $1/2$. With respect to the peaks, they are probably caused by the complex interaction between the filter size length (here 3), dp and other convolutional settings (e.g., stride and padding) and the use of a smaller domain for learning than for generation. In addition, the facies fractions in the TI are moderately well reproduced by the average over 100 realizations: facies 0: 0.596 versus 0.546, facies 1: 0.119 versus 0.147, and facies 2: 0.285 versus 0.307.

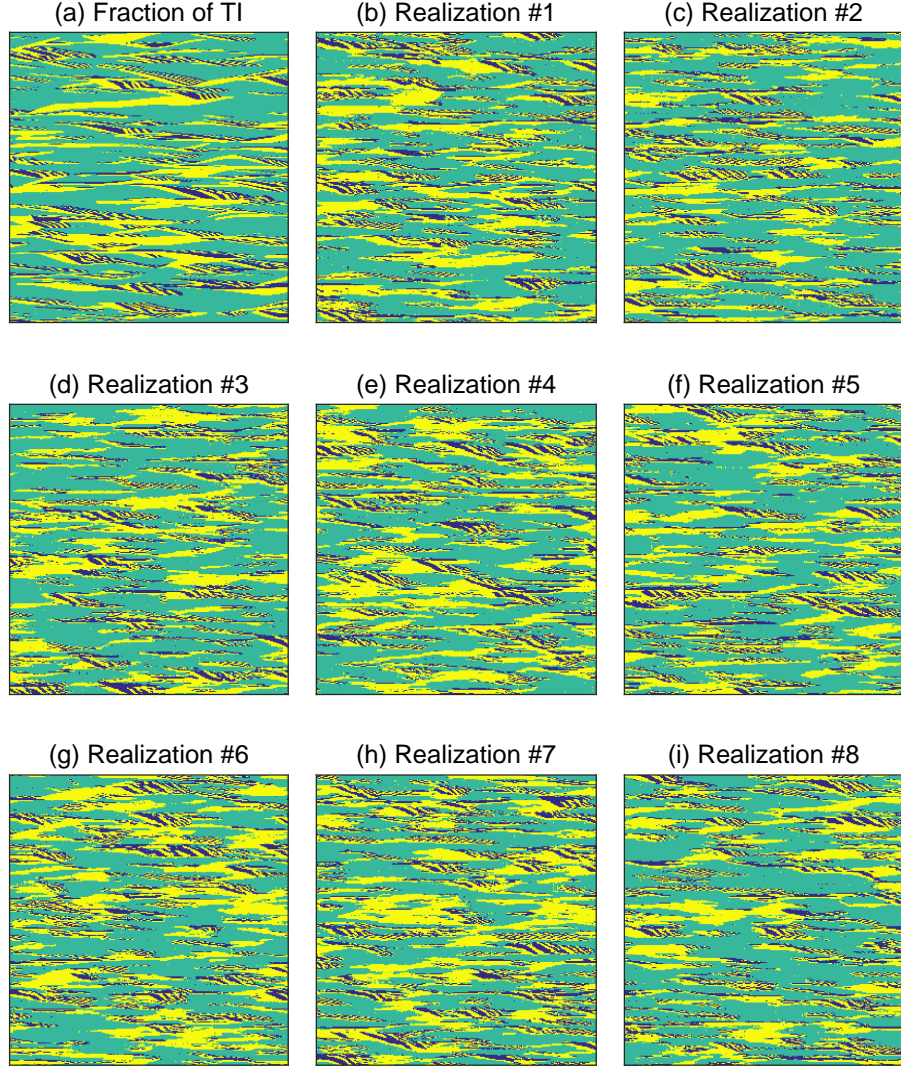


Figure 6: (a) Fraction of size 289×289 of the TI shown in Figure 2b and (b) - (i) randomly chosen 289×289 realizations derived by our SGAN. Each realization is generated by sampling 300 random numbers from a uniform distribution, $U(-1, 1)$.

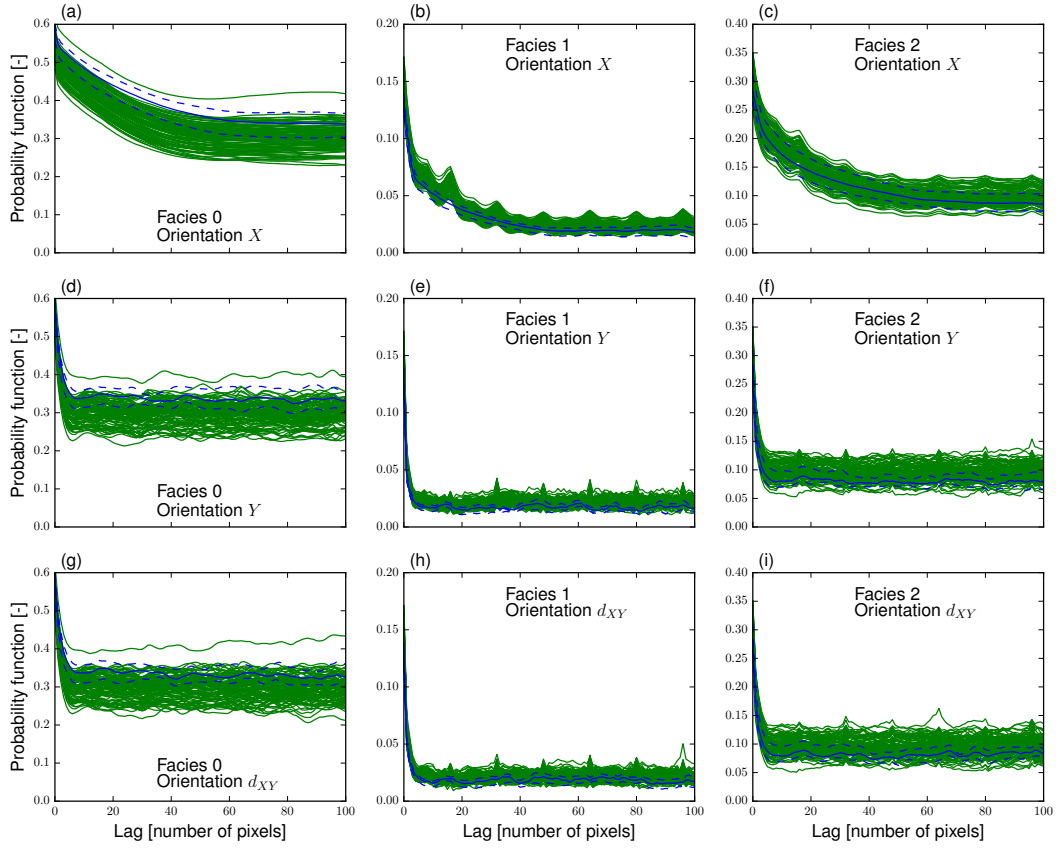


Figure 7: Probability function (PF) for the 2D case study involving the tri-categorical braided river aquifer TI depicted in Figure 2b. The blue lines refer to 100 randomly selected patches of size 289×289 from the 400×400 TI with the solid blue line indicating the mean and the 2 dashed lines representing the minimum and maximum values at each lag. The green solid lines represent 100 SGAN realizations of size 289×289 . The PF is calculated for each facies along spatial directions. The x and y symbols signify the x and y axes, and d_{xy} represents the diagonal direction formed by the 45° angle between the x and y axes.

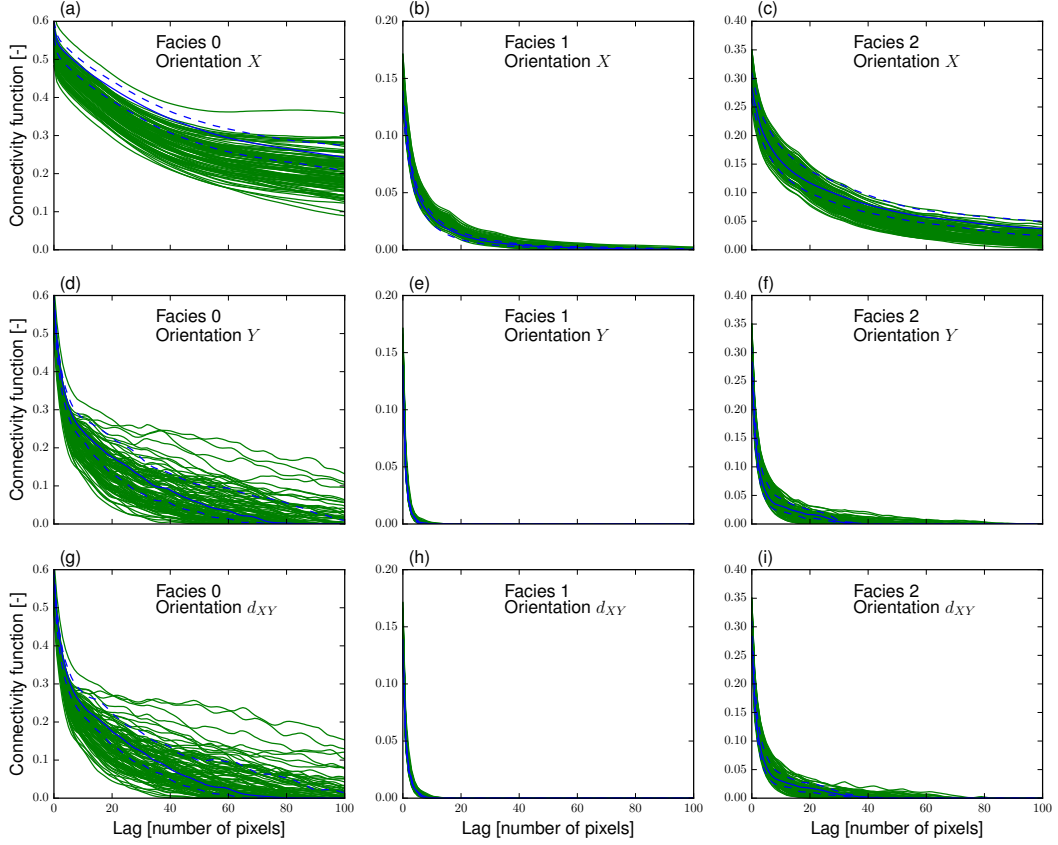


Figure 8: Cluster or connectivity function (CF) for the 2D case study involving the tri-categorical braided river aquifer TI depicted in Figure 2b. The blue lines refer to 100 randomly selected patches of size 289×289 from the 400×400 TI with the solid blue line indicating the mean and the 2 dashed lines representing the minimum and maximum values at each lag. The green solid lines represent 100 SGAN realizations of size 289×289 . The CF is calculated for each facies along spatial directions. The x and y symbols signify the x and y axes, and d_{xy} represents the diagonal direction formed by the 45° angle between the x and y axes.

For this case study, we performed a comparison between our trained SGAN and the well-established DeeSse (DS) MPS algorithm (*Mariethoz et al., 2010*). Using the standard setting of a maximum number of neighboring nodes, nn_{\max} , of 30, together with a large search radius of 120 pixels and a distance threshold of 0.01 (see *Mariethoz et al., 2010*, for details about these algorithmic parameters), producing one model realization incurs a computational cost of 417 s on the used machine. As shown in Figures 9b and 9c, the resulting realizations strongly deviate from the TI. Increasing nn_{\max} to 75 leads to a CPU-time per realization of 1180 s. The corresponding realizations now look more similar to the TI (Figure 9d-i) and their facies proportions are close to those of the TI: facies 0: 0.594, facies 1: 0.118 and facies 2: 0.288. Yet the associated PF and CF statistics generally do not match those of the TI (Figures 10 and 11). In contrast, after training our SGAN incurs a CPU-time per realization of only 0.1 s on the same

machine, which is thus more than 10,000 times less than for DS. Furthermore, despite the unwanted peaks described above our SGAN produces more consistent PF and CF statistics (compare Figures 7 and 8 against Figures 10 and 11, respectively).

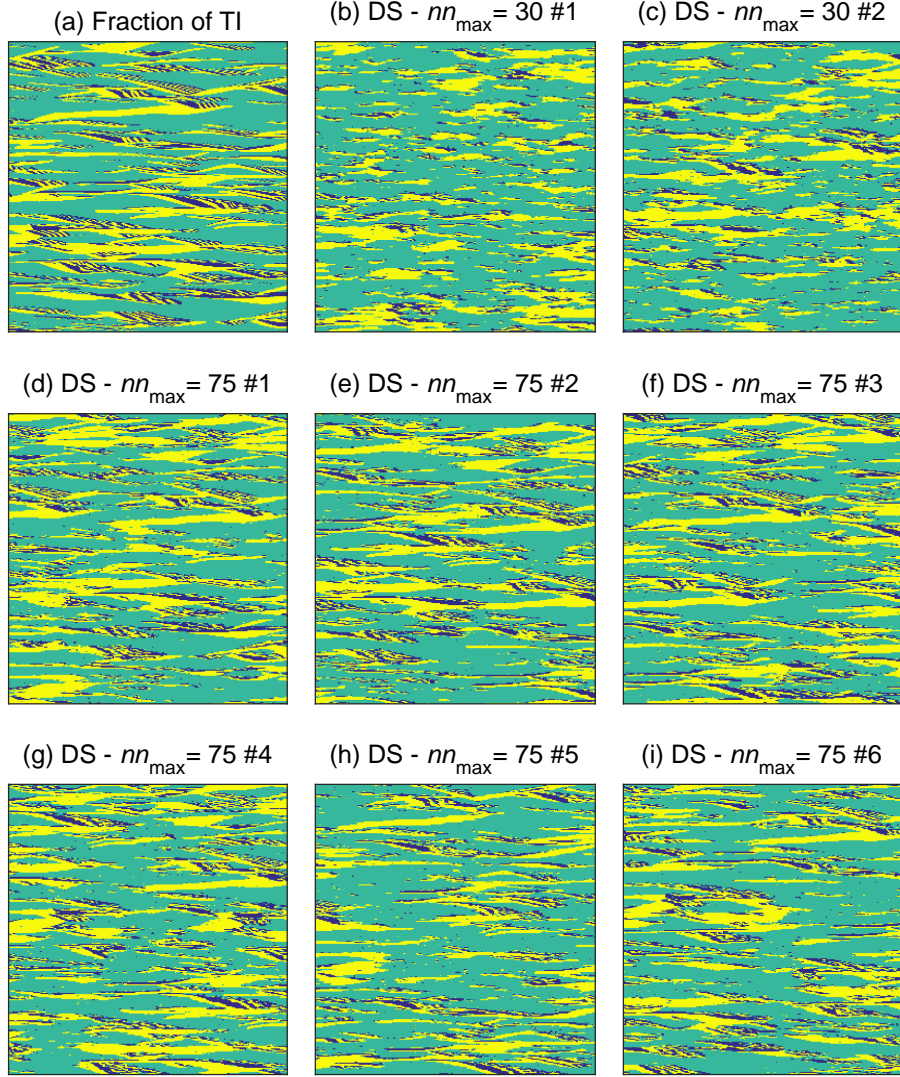


Figure 9: (a) Fraction of size 289×289 of the TI shown in Figure 2b, and (b) - (c) randomly chosen 289×289 realizations derived by the DS algorithm with a maximum number of neighboring nodes (nn_{\max} of 30, and (d)-(i) randomly chosen 289×289 realizations derived by the DS algorithm with $nn_{\max} = 75$. On the used machine, the CPU-time per DS realization was 417 s for $nn_{\max} = 30$ and 1180 s for $nn_{\max} = 75$.

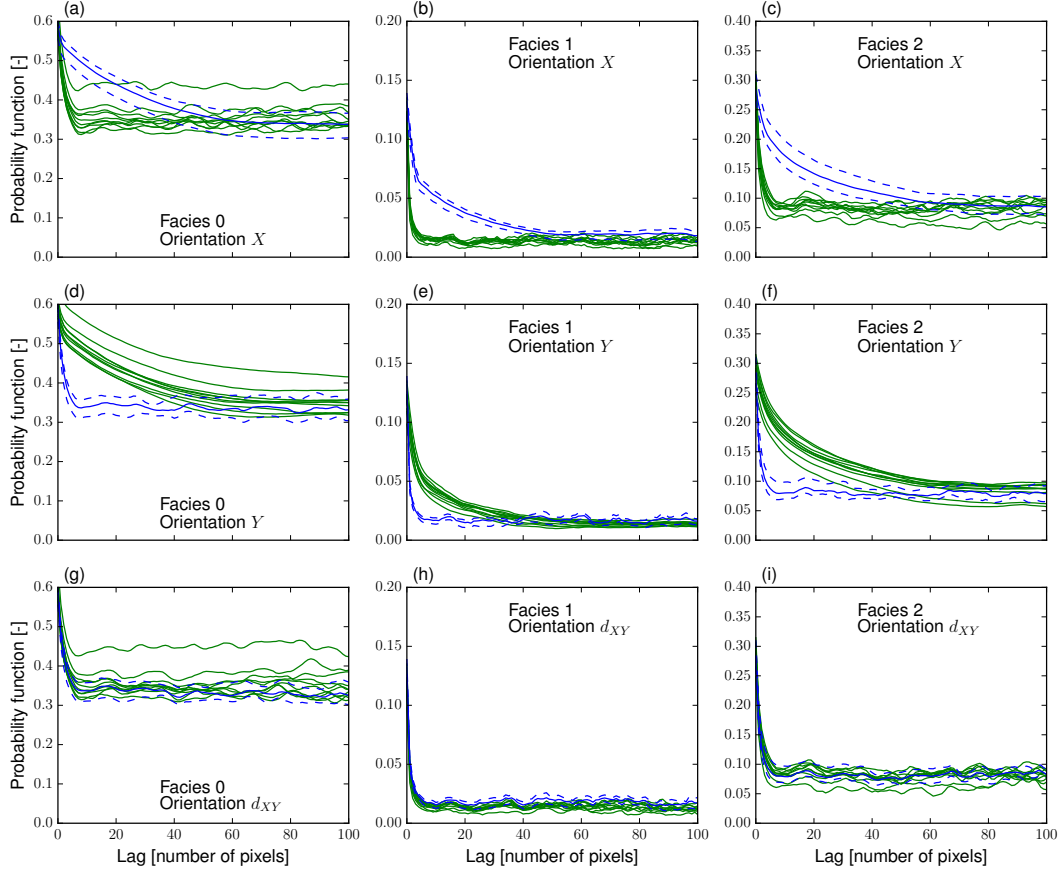


Figure 10: Probability function (PF) obtained when running the DS algorithm for the 2D case study involving the tri-categorical braided river aquifer TI depicted in Figure 2b. The blue lines refer to 100 randomly selected patches of size 289×289 from the 400×400 TI with the solid blue line indicating the mean and the 2 dashed lines representing the minimum and maximum values at each lag. The green solid lines represent 10 realizations of size 289×289 derived by DS with the nn_{\max} parameter set to 75. Only 10 realizations were generated given the large CPU-time per realization inherent to DS for this case study. The PF is calculated for each facies along spatial directions. The x and y symbols signify the x and y axes, and d_{xy} represents the diagonal direction formed by the 45° angle between the x and y axes.

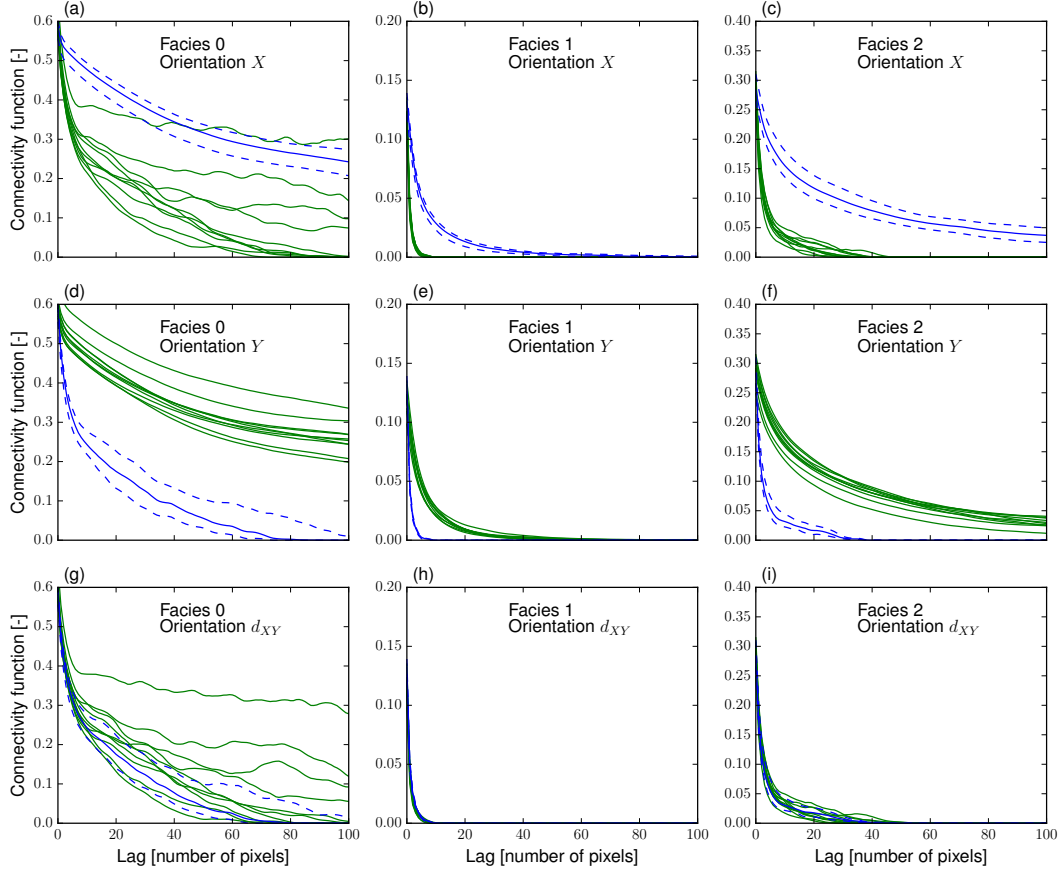


Figure 11: Cluster or connectivity function (CF) obtained when running the DS algorithm for the 2D case study involving the tri-categorical braided river aquifer TI depicted in Figure 2b. The blue lines refer to 100 randomly selected patches of size 289×289 from the 400×400 TI with the solid blue line indicating the mean and the 2 dashed lines representing the minimum and maximum values at each lag. The green solid lines represent 10 realizations of size 289×289 derived by DS with the nn_{\max} parameter set to 75. Only 10 realizations were generated given the large CPU-time per realization inherent to DS for this case study. The CF is calculated for each facies along spatial directions. The x and y symbols signify the x and y axes, and d_{xy} represents the diagonal direction formed by the 45° angle between the x and y axes.

3.2 3D Models

Our first 3D case study relies on the $340 \times 200 \times 80$ binary TI shown in Figure 2c. This TI represents the hydrofacies in an alluvial aquifer in the Maules Creek valley, Australia (available at <http://www.trainingimages.org/training-images-library.html>). At learning time we used $z_x = 2$ and $q = 3$, thereby resulting in a patch size of $33 \times 33 \times 33$. Also, because of GPU memory limitations each training batch contained 32 patches. The analyzed realizations were created using $z_x = 4$ and $q = 3$. This corresponds to a 192-dimensional \mathbf{Z} and produces realizations of size $97 \times 97 \times 97$. The selected 3D SGAN network was that obtained after 50 training epochs. Median filtering with a kernel size

of $(3, 1, 1)$ was used before thresholding at the 0.5 level.

Figure 12 shows 8 (randomly chosen) realizations, together with a fraction of the TI. Both the $97 \times 97 \times 97$ realizations and the $340 \times 200 \times 80$ TI were cropped to $80 \times 80 \times 80$ for visual convenience. The realizations display overall similar patterns as the TI. Figure 13 provides more insights into the comparison. The 25 realizations describe well the trend found in the TI for the PF (Figure 13) and CF (not shown). Here we do not show the CF statistics as they are almost identical to the depicted PF statistics. This is caused by the presence of large connected features. Basically, if two voxels separated by a given lag belong to the same facies (as expressed by the PF), then it is extremely likely that they are connected (as expressed by the CF). The spread in the realization is larger than for the TI but again this is expected as the TI's metrics are not independent: the ratio of the size of a TI's patch to the size of the TI is about $1/11$. More importantly, the PF and CF (not shown) of the realizations show regular bumps and valleys that are not present in the TI. The distance between two such peaks is about 20 voxels. Similarly as for the realizations' PF in our second 2D case study (Figure 7), we suspect that this is caused by a complex interaction between the used convolutional settings and the chosen domain size. As of facies fractions, the average over the 25 realizations perfectly honors the TI with a proportion of matrix voxels of 0.51 in both cases.

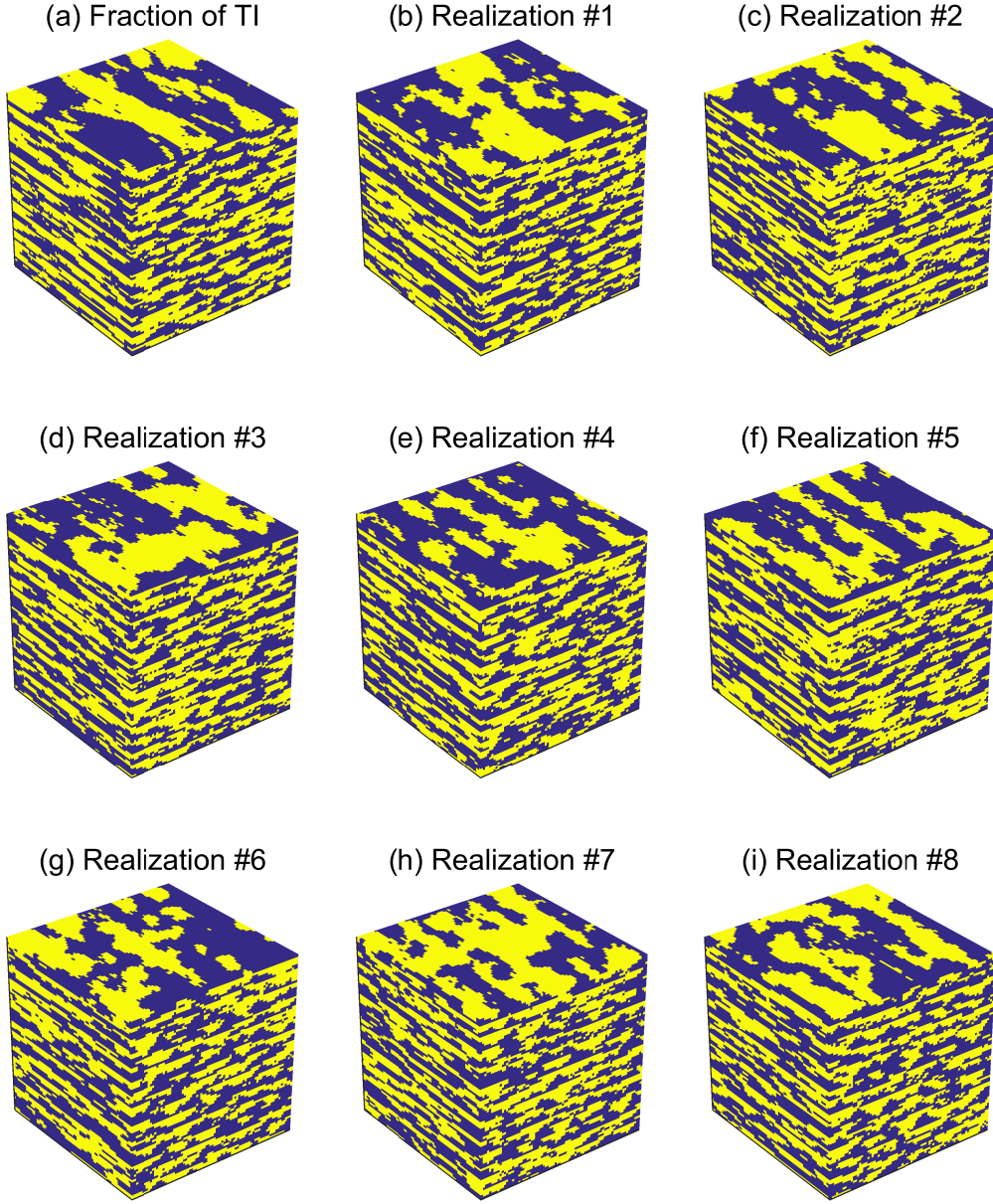


Figure 12: (a) Fraction of size $80 \times 80 \times 80$ of the TI shown in Figure 2c and (b) - (i) randomly chosen $80 \times 80 \times 80$ realizations derived by our 3D SGAN. Each realization is generated by sampling 192 random numbers from a uniform distribution, $U(-1, 1)$. The $340 \times 200 \times 80$ TI and original $97 \times 97 \times 97$ realizations (see main text for details) were all cropped to $80 \times 80 \times 80$ for visual convenience.

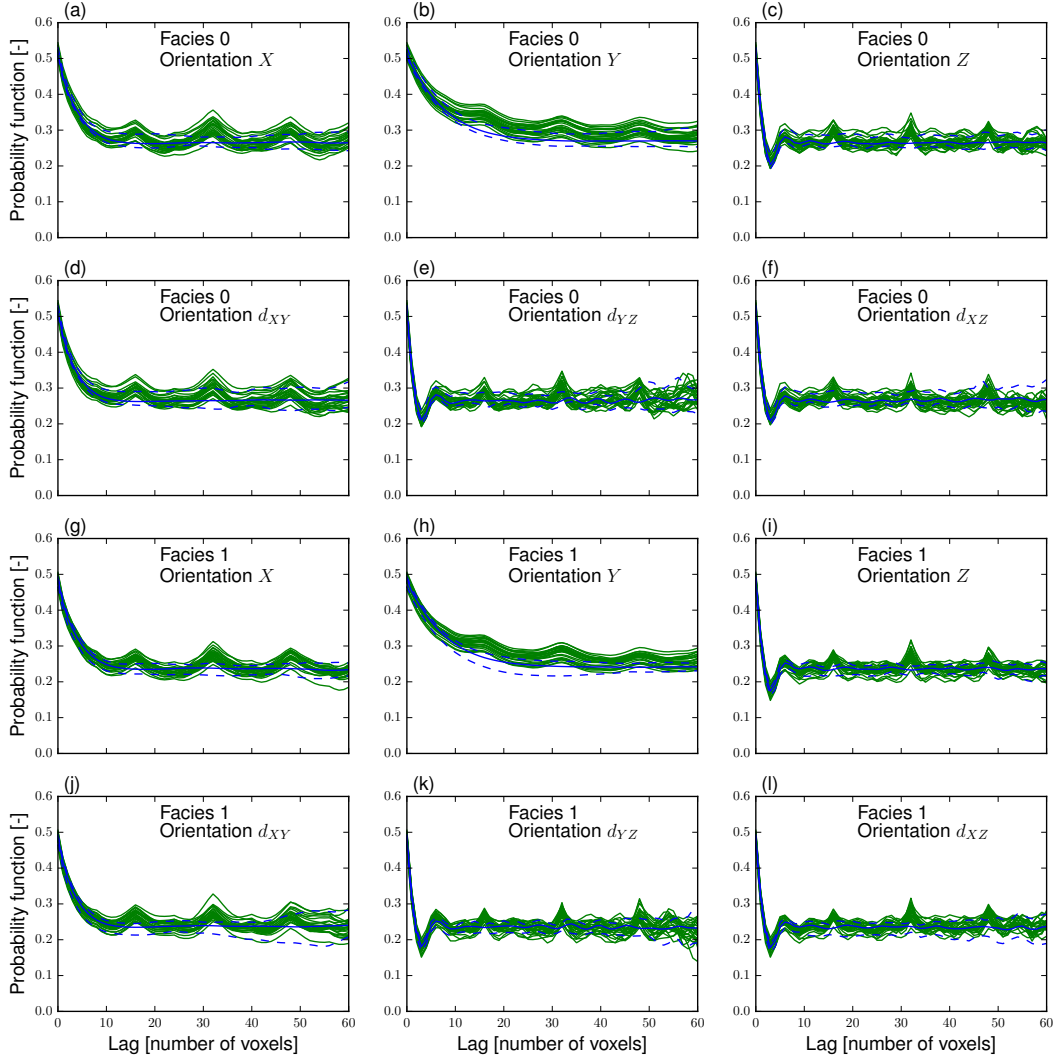


Figure 13: Probability function (PF) for the 3D case study involving the binary Maules Creek alluvial aquifer TI depicted in Figure 2c. The blue lines refer to 25 randomly selected patches of size $80 \times 80 \times 80$ from the $340 \times 200 \times 80$ TI with the solid blue line indicating the mean and the 2 dashed lines representing the minimum and maximum values at each lag. The green solid lines represent 25 SGAN realizations of size $80 \times 80 \times 80$. The PF is calculated for each facies along spatial directions. The x , y and z symbols signify the x , y and z axes. The d_{xy} , d_{yz} and d_{xz} symbols represent the diagonal directions formed by the 45° angle from the x -axis in the xy plane, from the y -axis in the yz plane and from the x -axis in the xz plane, respectively. Note that due to the presence of large connected features, the output of the cluster or connectivity function (CF) is almost identical to the displayed PF's output for this case study.

Our second 3D case study considers the $180 \times 150 \times 120$ categorical fold TI depicted in Figure 2d (and available at <http://www.trainingimages.org/training-images-library>).

html). Here we used $z_x = 4$ and $q = 1$ for training, together with a training batch size of 25. This implies using twenty-five $97 \times 97 \times 97$ random patches to build the training set associated with each epoch. In contrast, $z_x = 5$ and $q = 1$ were chosen to generate the realizations. This signifies that $129 \times 129 \times 129$ realizations are produced from a 125-dimensional, that is, $5 \times 5 \times 5$, \mathbf{Z} array. Furthermore, the selected 3D SGAN model was obtained at epoch 16 and median filtering with a $(3, 3, 3)$ kernel size was applied to the realizations before thresholding at the 0.5 level.

The TI and 8 (randomly chosen realizations) are presented in Figure 14, where the $180 \times 150 \times 120$ TI and every $129 \times 129 \times 129$ model realization was cropped to $120 \times 120 \times 120$ for visual convenience. The realizations show similar patterns as the TI rather well despite a slight over-representation of broken channels and the rare occurrence of small isolated patches. Also, the PF (Figure 15) and CF (not shown) statistics of the TI are rather well matched by the realizations while no proper comparison can be made between the respective spreads of the realizations and the TI's patches as these TI's patches are highly dependent. Indeed, the ratio of the size of a TI's patch to the size of the TI is about $1/2$ here. Similarly to the previous 3D case study, the presence of large connected features makes the outcome of the PF to be nearly identical to that of the CF. That is why the CF statistics are neither displayed for this case study. Lastly, the fraction of matrix voxels are 0.62 for the TI against 0.61 in average over the 25 realizations.

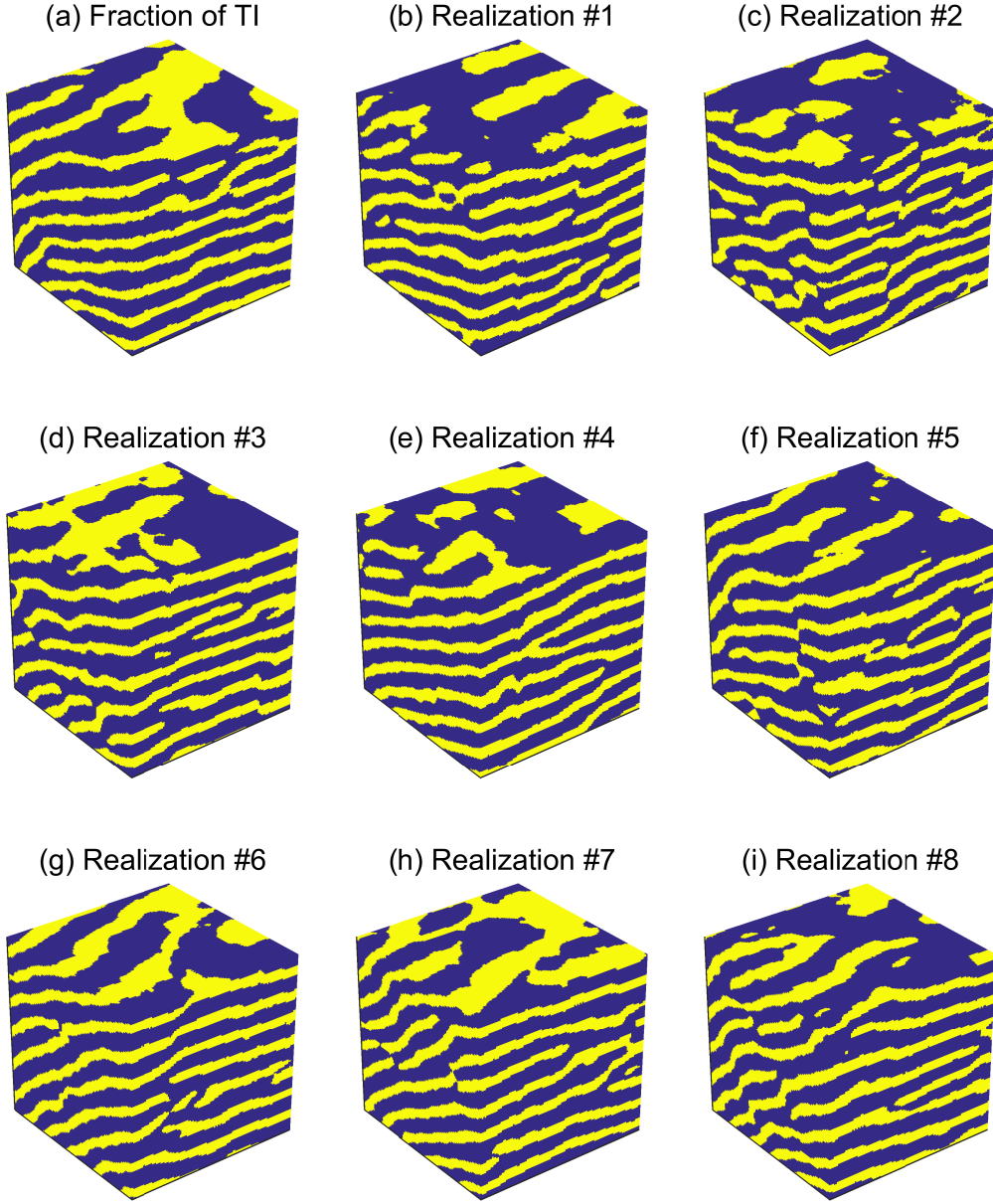


Figure 14: (a) Fraction of size $120 \times 120 \times 120$ of the TI shown in Figure 2d and (b) - (i) randomly chosen $120 \times 120 \times 120$ realizations derived by our 3D SGAN. Each realization is generated by sampling 125 random numbers from a uniform distribution, $U(-1, 1)$. The $180 \times 150 \times 120$ TI and original $129 \times 129 \times 129$ realizations (see main text for details) were all cropped to $120 \times 120 \times 120$ for visual convenience.

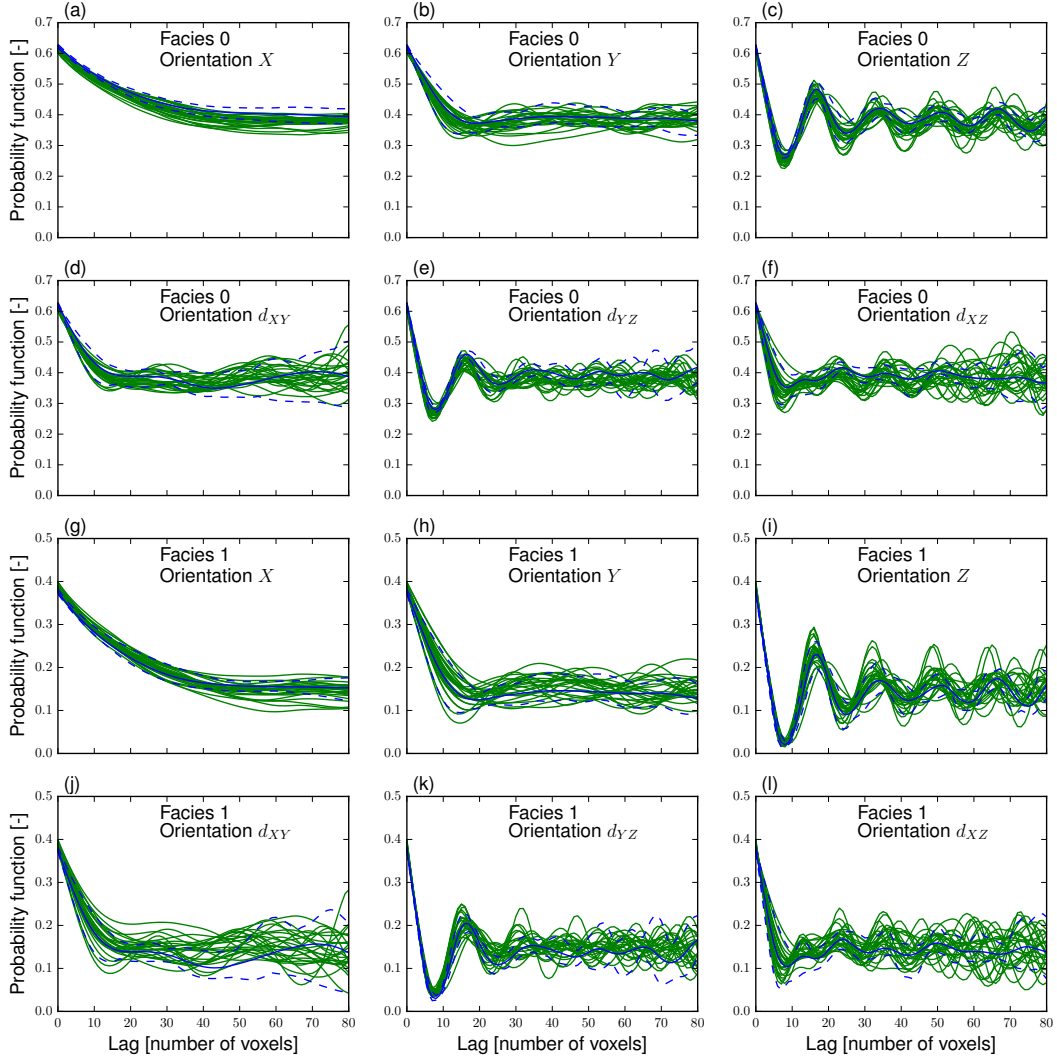


Figure 15: Probability function (PF) for the 3D case study involving the binary fold aquifer TI depicted in Figure 2d. The blue lines refer to 25 randomly selected patches of size $120 \times 120 \times 120$ from the $180 \times 150 \times 120$ TI with the solid blue line indicating the mean and the 2 dashed lines representing the minimum and maximum values at each lag. The green solid lines represent 25 SGAN realizations of size $120 \times 120 \times 120$. The PF is calculated for each facies along spatial directions. The x , y and z symbols signify the x , y and z axes. The d_{xy} , d_{yz} and d_{xz} symbols represent the diagonal directions formed by the 45° angle from the x -axis in the xy plane, from the y -axis in the yz plane and from the x -axis in the xz plane, respectively. Note that due to the presence of large connected features, the output of the cluster or connectivity function (CF) is almost identical to the displayed PF's output for this case study.

4 Inverse Problems

4.1 Case Study 1: 2D Steady-State Flow

Our first inversion case study considers 2D steady-state flow within a channelized aquifer that is consistent with the TI shown in Figure 2a. The total number of pixels is $125 \times 125 = 15,625$, and the 125×125 aquifer domain lies in the $x - y$ plane with a grid cell size of 1 m and a thickness of 1 m. Channel and matrix materials (see Figure 16a) are assigned hydraulic conductivity values of 1×10^{-2} m/s and 1×10^{-4} m/s, respectively. MODFLOW 2005 (Harbaugh, 2005) is used to simulate steady state groundwater flow with no flow boundaries at the upper and lower sides and a lateral head gradient of 0.01 (-) with water flowing in the x -direction. Water is extracted at a rate of $0.001 \text{ m}^3/\text{s}$ by a well located at the center of the domain. The measurement data were formed by acquiring simulated heads at 49 locations that are regularly spread over the domain (Figure 16a). A Gaussian white noise with standard deviation of 0.01 m was then used to corrupt these data. For the selected white noise realization, the measurement data have a root-mean-square-error (RMSE) of 0.0096 m. The corresponding signal-to-noise-ratio (SNR), defined as the ratio of the average RMSE obtained by drawing prior realizations with our SGAN algorithm to the noise level is as large as 44. Figures 16b-i depict 8 (randomly chosen) prior realizations. It can be seen that prior variability is quite large.

The reference model (Figure 16a) was generated using our SGAN approach. This was achieved by randomly drawing a 25-dimensional (5×5) $\boldsymbol{\theta} = \mathbf{Z} \sim U(-1, 1)$, which results in a 129×129 model realization (see equation 3). The obtained realization was cropped to 125×125 to form the reference model while the models generated during the MCMC sampling were similarly cropped. The DREAM_(ZS) sampler was ran in parallel, using 8 interacting Markov chains distributed over 8 CPUs. Uniform priors in the $[-1, 1]$ range were selected for the 25-dimensional $\boldsymbol{\theta}$.

The chains start to jointly sample the posterior distribution, $p(\boldsymbol{\theta}|\mathbf{d})$, after a (serial) total of approximately 96,000 iterations, that is, 12,000 parallel iterations per chain (not shown). The sampled realizations closely resemble the true model and the posterior variability is rather small (Figure 17). After a total of 387,200 MCMC iterations, that is, 48,400 iterations in each chain, the Gelman and Rubin (1992) convergence diagnostic, \hat{R} , is satisfied (i.e., $\hat{R} \leq 1.2$) for every sampled parameter (see, e.g., Laloy et al., 2015, for details about the use of \hat{R} with DREAM_(ZS)).

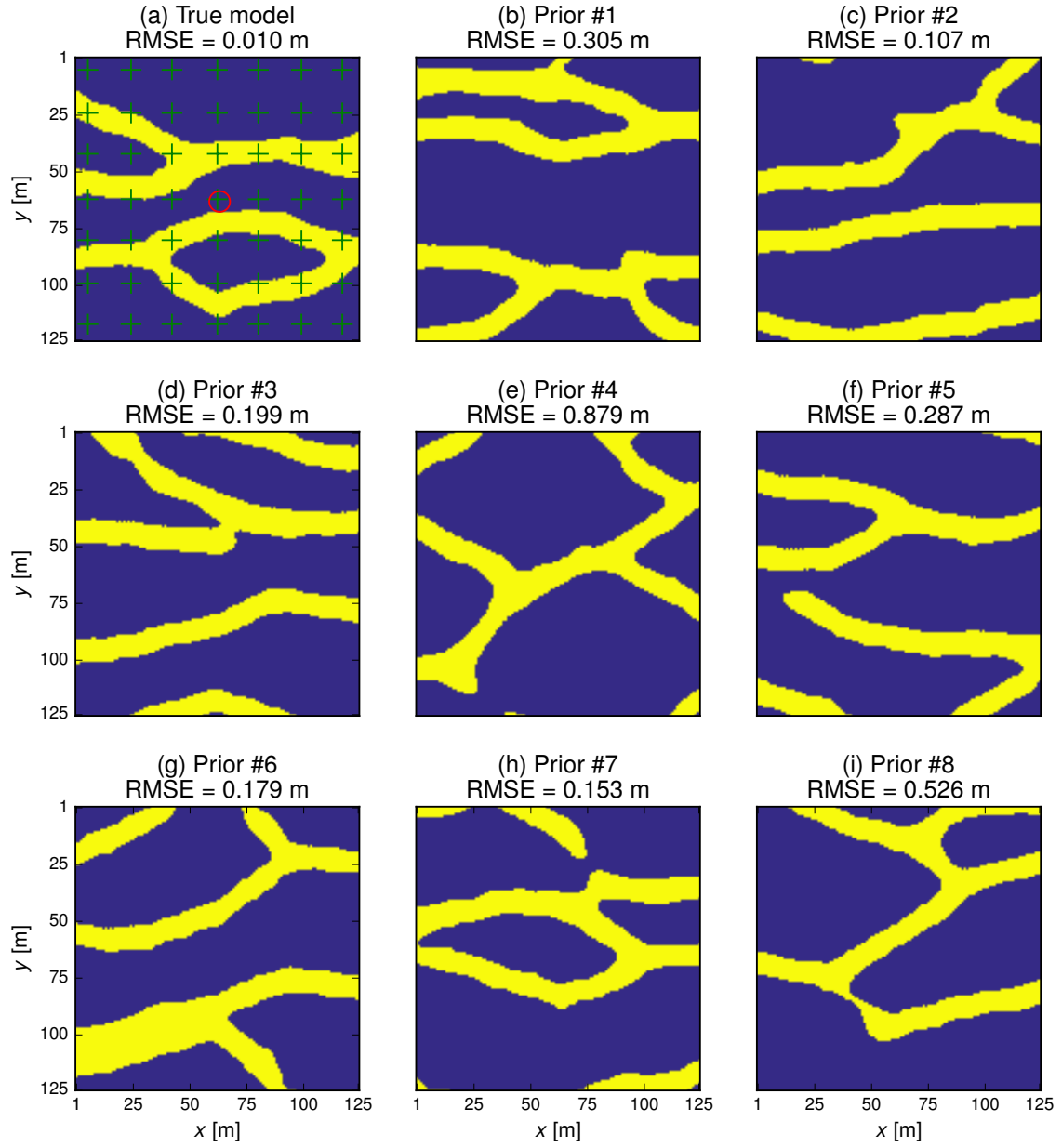


Figure 16: (a) True model and (b-i) eight randomly chosen prior realizations. The red circle and green crosses in subfigure (a) mark the location of the pumping well and the piezometers, respectively. The models' dimensions are 125×125 .

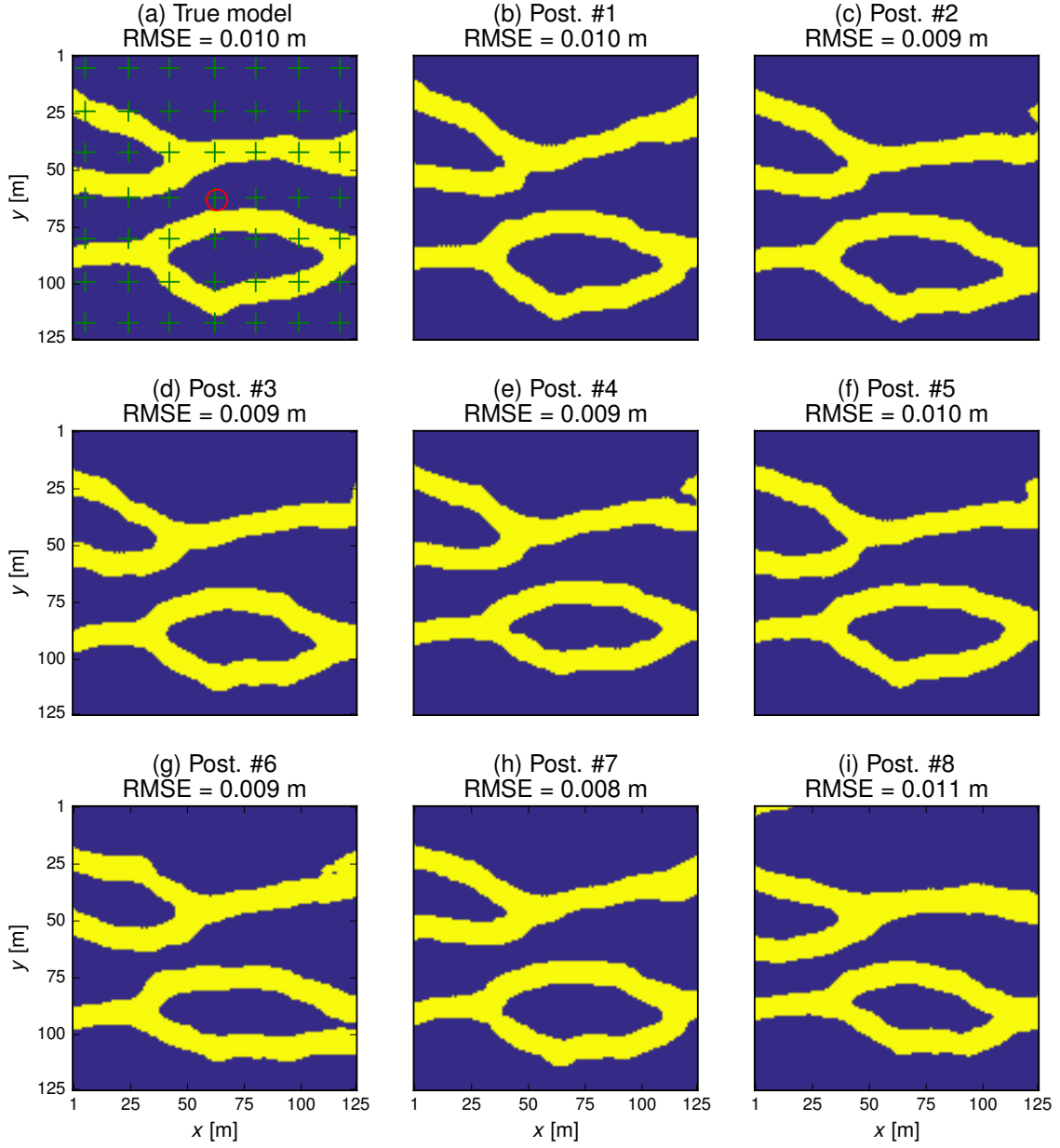


Figure 17: (a) True model and (b-i) eight randomly chosen posterior realizations derived by DREAM_(ZS). The red circle and green crosses in subfigure (a) mark the location of the pumping well and the piezometers, respectively. The models' dimensions are 125×125 .

4.2 Case Study 2: 3D Transient Hydraulic Tomography

Our last case study consists of a 3D transient hydraulic tomography example (e.g., *Cardiff et al.*, 2013). Transient head variations induced by discrete multilevel pumping

tests were simulated using MODFLOW2005 within a 3D confined aquifer of size $30 \times 61 \times 61$ with a voxel size of $1 \text{ m} \times 1 \text{ m} \times 1 \text{ m}$. The total number of voxel values is thus $30 \times 61 \times 61 = 111,630$. The considered aquifer honors the categorical fold TI presented in Figure 2d. The true model is depicted in Figure 18a. It was obtained by feeding our 3D SGAN with a randomly drawn 27-dimensional $(3 \times 3 \times 3)$ $\boldsymbol{\theta} = \mathbf{Z} \sim U(-1, 1)$. This creates models of size $65 \times 65 \times 65$ (equation 3) that are subsequently cropped to $30 \times 61 \times 61$.

Channel and matrix materials are assigned hydraulic conductivity values of 1×10^{-4} m/s and 1×10^{-6} m/s, respectively. The multilevel discrete pumping setup includes a 30-m deep, central multi-level well in which water is sequentially extracted every 4 m along a 1-m long screen (at depths of 3, 7, 11, 15, 19, 23 and 27 m respectively) during 30 minutes at a rate of 10 liters/min. This central well is surrounded by 8 multilevel piezometers where drawdowns are recorded every 4 m along a 1-m long screen during each pumping sequence. Locations of the multilevel pumping well, the 8 multilevel observation wells and their associated screens are displayed in Figure 19. For each drawdown curve, data collected at the same four measurement times were selected, leading to a total of $8 \times 7 \times 7 \times 4 = 1568$ measurement data. These measurement times were considered to be the four most informative ones after visual inspection of several drawdown curves (not shown). These data were corrupted with a Gaussian white noise using again a standard deviation of 0.01 m. For the chosen white noise realization, this caused a RMSE of 0.0099 m and the associated SNR is 22. Prior variability is large, with prior models having RMSE values that are 15 to 28 times larger than that of the true model. Given the involved nonlinearities, the large number of measurement data (1568) and the relatively large SNR (22), we deem this inverse problem to be quite challenging.

For this case study, the DREAM_(ZS) sampler evolves again 8 Markov chains in parallel using 8 CPUs while uniform priors in $[-1, 1]$ are assumed for the 27 dimensions of $\boldsymbol{\theta}$. The allowed computational expense was 50,000 iterations per chain, which represents a computing time of 6.5 days on the used 8-core workstation. After consumption of this budget, the 8 chains converge towards a data misfit in the range of 0.0105 m - 0.0110 m (Figures 18b-i). This interval is close to the target level of 0.0099 m. This indicates that the posterior mode has not been quite sampled yet. The variability among the sampled models is rather small (Figures 18b-i). This is likely due to the combination of two factors: (1) the peakedness of the likelihood function (equation (11)) caused by the large number of measurement data with small noise, and (2) the difficulties encountered by the MCMC algorithm for exploring this complex target distribution. Nevertheless, the recovered models (Figures 18b-i) are visually rather close to the true model (Figure 18a).

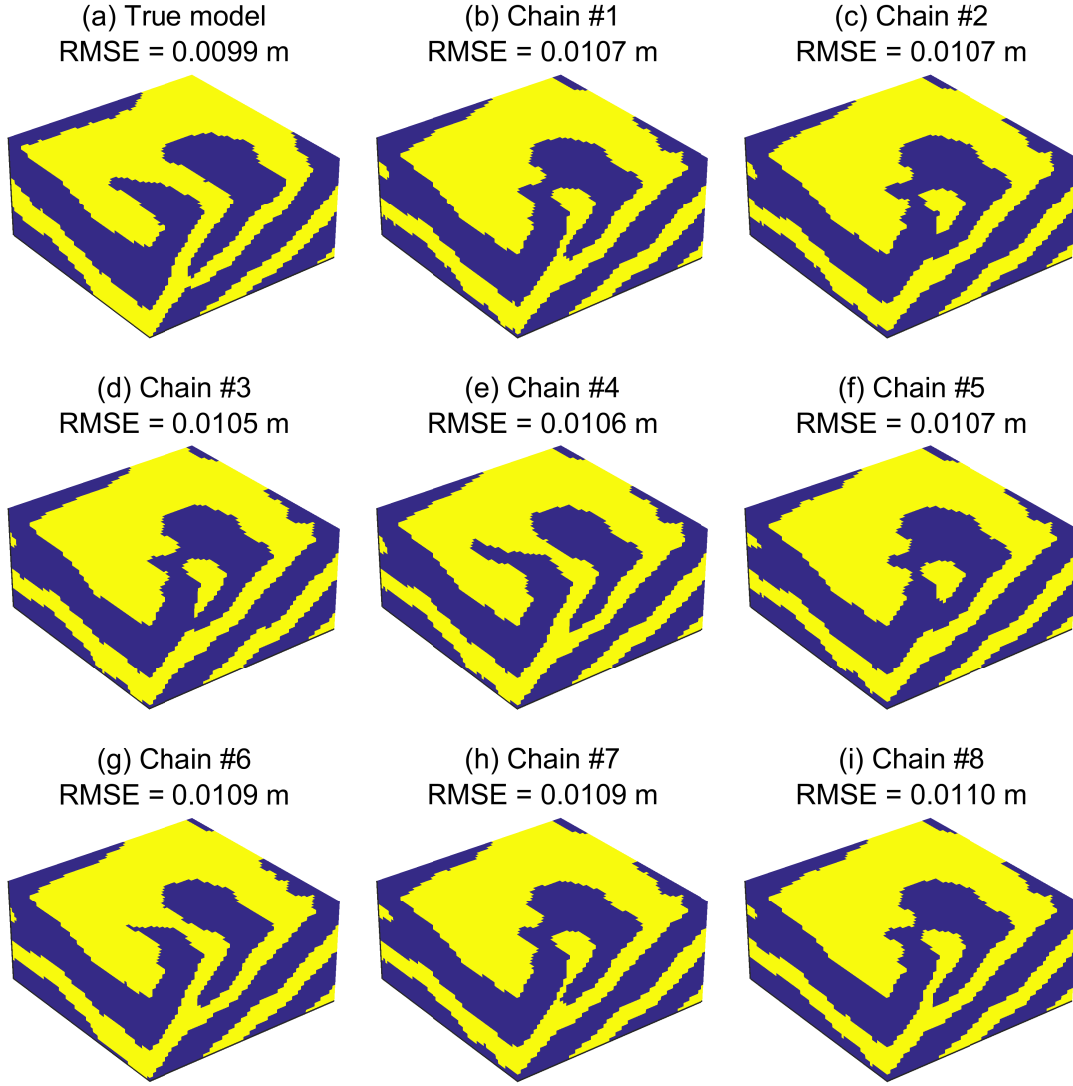


Figure 18: a) True model and (b-i) states of the 8 Markov chains evolved by $\text{DREAM}_{(\text{ZS})}$ after 50,000 iterations per chain for the inverse case study 2 (see section 4.2). The models' dimensions are $30 \times 61 \times 61$.

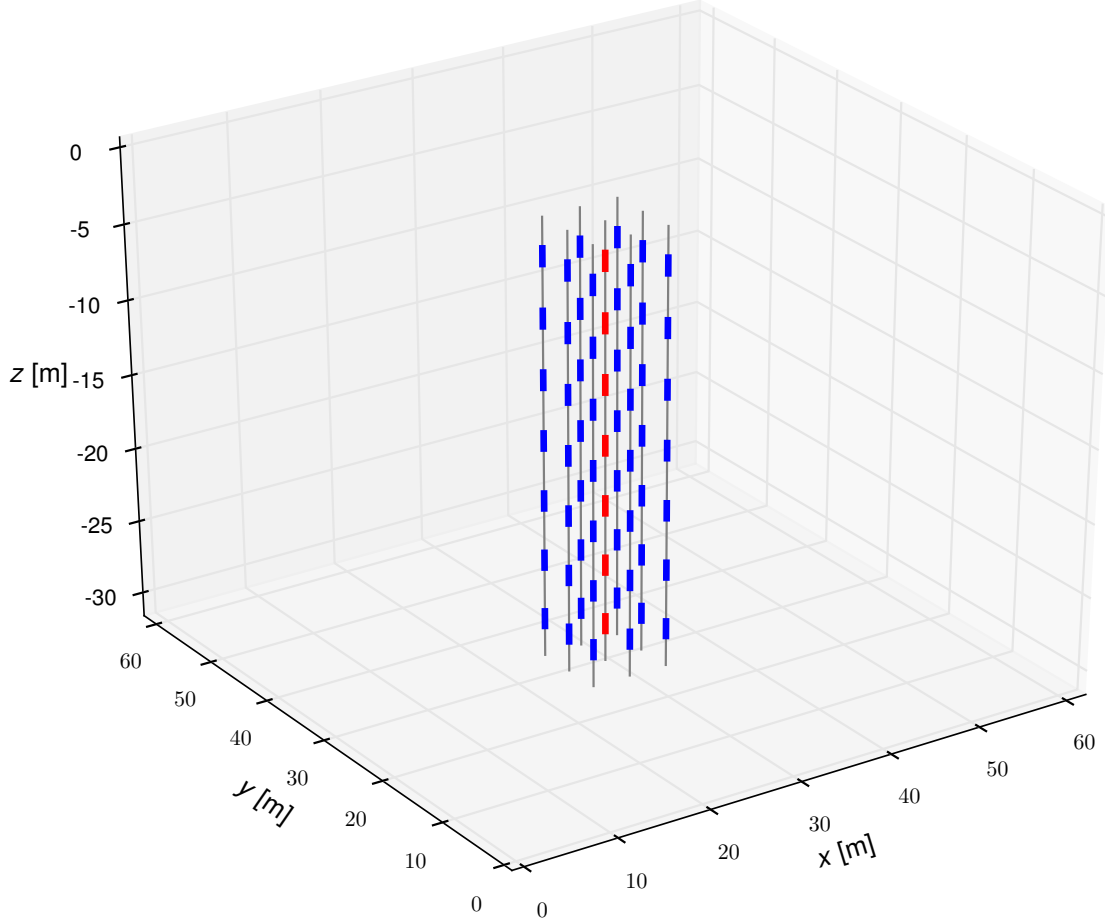


Figure 19: Pumping and observation locations in the synthetic 3D hydraulic tomography setup. The vertical gray lines represent the multilevel pumping and observation wells. The red line segments in the central well are the pumping locations and the blue line segments in the other wells are the head measurement locations. The vertical direction (z -axis) is exaggerated by a factor 2.

5 Discussion

Altogether, our results demonstrate that our proposed SGAN-based inversion approach works well. Compared to our previous work with a totally different type of neural network (*Laloy et al.*, Under Review), the current study solves three important issues: it relies on a single TI, can deal with multi-categorical TIs and builds a low-dimensional representation where each independent low-dimensional variable only influences a specific region of the

generated model realization. The latter point allows us to solve inverse problems that have smaller noise and larger dimensionality compared to those considered in *Laloy et al.* (Under Review). In addition, our proposed approach has one more advantage for inversion: it permits an even larger compression ratio. The latter can be above 10,000 for a 3D binary channelized aquifer. Yet for our synthetic 3D transient hydraulic tomography the posterior distribution was not appropriately sampled. Using more than 8 parallel DREAM_(ZS) chains and letting the MCMC sampling continue beyond 50,000 MCMC iterations per parallel chain would likely help in this respect.

Although our main goal is inversion, we consider that our 2D/3D SGAN also shows a lot of promise for unconditional geostatistical simulation. Its main advantage is speed: as stated earlier 3D model realizations containing some two millions of grid cells can be generated in less than 3 seconds on a standard desktop computer (after the network is learned). Furthermore, a comparison against the DeeSse code (DS, *Mariethoz et al.*, 2010) for the 400×400 braided river tri-categorical TI (depicted in Figure 2b) reveals that for this particular case study, our SGAN generates more consistent realizations and incurs a 10,000 times smaller computational time per realization (after training of the neural network).

The main limitation of our proposed approach is that direct conditioning to point data cannot be done. For geostatistical simulation, a possible solution to this problem consists of (1) train the network, (2) produce a realization, $\hat{\mathbf{X}}$, from a given low-dimensional \mathbf{Z} vector and (3) optimize the values in \mathbf{Z} such that $\hat{\mathbf{X}}$ honors the available conditioning point data. Limited testing in this direction shows encouraging results although the induced computational overhead needs to be reduced. For inversion, \mathbf{Z} cannot be modified after its creation by the inversion algorithm. A potential alternative could therefore be to match the direct conditioning data as a second term in the likelihood function (objective function).

Even if not considered or demonstrated herein, we would like to stress that our 2D/3D SGAN can be trained on continuous TIs as well. Figure 20 displays model realizations obtained by our 3D SGAN for the continuous version of the 3D categorical fold depicted in Figure 2d (a fraction of this continuous TI is shown in Figure 20a). These $129 \times 129 \times 129$ realizations were obtained using $z_x = 5$ and $q = 3$, that is, a 375-dimensional \mathbf{Z} . Also, a rank transformation was used to better mimic the continuous range found in the TI: the continuous values in the realizations were ranked and replaced by values with equal rank in the TI. Though far from perfect, we believe these results are promising.

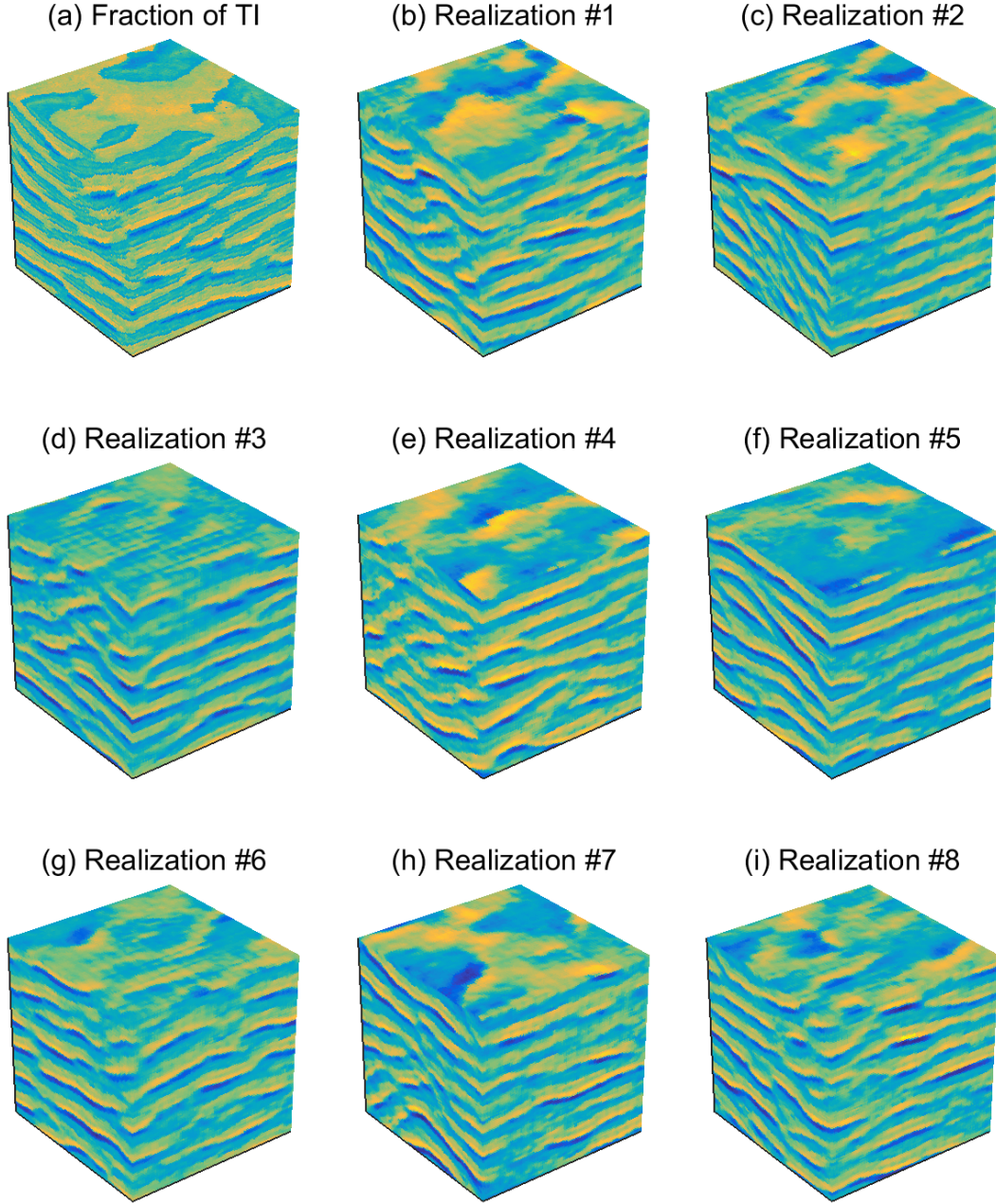


Figure 20: (a) Fraction of size $120 \times 120 \times 120$ of the $180 \times 150 \times 120$ continuous fold TI (available at <http://www.trainingimages.org/training-images-library.html>) and (b) - (i) randomly chosen $120 \times 120 \times 120$ realizations derived by our 3D SGAN. Each realization is generated by sampling 375 random numbers from a uniform distribution, $U(-1, 1)$. The $180 \times 150 \times 120$ TI and original $129 \times 129 \times 129$ realizations (see main text for details) were all cropped to $120 \times 120 \times 120$ for visual convenience.

6 Conclusion

We present a new training-image based simulation and inversion approach for complex geologic media that relies on a deep neural network of the spatial generative adversarial network (SGAN) kind. Our proposed SGAN can generate 2D and 3D unconditional realizations from a categorical training image (TI) and, in principle, a continuous TI as well. Compared to existing geostatistical methods, it has the advantage that it allows for a high degree of geological realism using a (very) low-dimensional representation of the original model domain, thereby allowing for efficient probabilistic (or deterministic) inversion. After training, generating a realization is also very fast. For instance, a 3D binary channelized model containing more than 2 million voxels can be generated in less than 3 seconds using a standard desktop computer, by randomly sampling a 125-dimensional uniform vector. Several 2D and 3D categorical TIs are used to study the unconditional simulation capabilities of our SGAN-based simulation approach. More importantly, synthetic inversion case studies involving 2D steady-state flow and 3D transient hydraulic tomography demonstrate the effectiveness of our SGAN for probabilistic inversion. For the 2D case, the inversion rapidly explores the posterior model distribution, while for the 3D case the inversion produces model realizations that fit the data close to the target level and look visually close to the true model. The main topics for future research is how to best include direct conditioning data and to thoroughly investigate application to continuous TIs.

Acknowledgments

Python codes of the proposed 2D/3D SGAN-based simulation and inversion approaches are available from the first author (and will be made available on <https://github.com/elaloy>). This work was partially supported by Agence Nationale de la Recherche through the grant ANR-16-CE23-0006 Deep in France. We thank the original 2D SGAN developers for sharing their code (https://github.com/ubergmann/spatial_gan). A temporary academic license of the DeeSse (DS) MPS code can be obtained upon request to one of its developers (Grégoire Mariethoz, Philippe Renard, Julien Straubhaar). Finally, we thank Laurent Lemmens for sharing his PF and CF calculation routines.

References

- Cardiff, M., W. Barrash, and P. K. Kitanidis (2013), Hydraulic conductivity imaging from 3-D transient hydraulic tomography at several pumping/observation densities, *Water Resources Research*, 49, 7311–7326. <http://dx.doi.org/10.1002/wrcr.20519>.
- Dieleman, S., J. Schlüter, C. Raffel, E. Olson, S. K. Sønderby, D. Nouri, D. Maturana, M. Thoma, E. Battenberg, J. Kelly, J. De Fauw, M. Heilman, D. Moitinho de Almeida, B. McFee, H. Weideman, G. Takács, P. de Rivaz, J. Crall, G. Sanders, R. Kashif, C. Liu, G. French, and J. Degraeve (2016), LASAGNE: First release, August 2015. <http://dx.doi.org/10.5281/zenodo.27878>.
- Dumoulin, V., and F. Visin (2016), A guide to convolution arithmetic for deep learning, *arXiv:1603.07285v1*, [stat.ML], 23 March 2016.
- Gelman A. G, and D. N Rubin (1992), Inference from iterative simulation using multiple sequences, *Statistical Science*, 7, 457–472.
- Gómez-Hernández, J. J, and X.-H. Wen X-H (1998), To be or not to be multi-Gaussian? A reflection on stochastic hydrogeology, *Advances in Water Resources*, 21(1), 47–61.

- Goodfellow, I., J. Pouget-Abadie, M. Mirza, B. Xu, D. Warde-Farley, S. Ozair, A. Courville, and Y. Bengio (2014), Generative adversarial networks, *The Annual Conference on Neural Information Processing Systems (NIPS)*, Montréal.
- Goodfellow, I., Y. Bengio, A. Courville (2016), *Deep learning*, MIT Press. <http://www.deeplearningbook.org>.
- Harbaugh, A. W (2005), MODFLOW-2005, the U.S. Geological Survey modular groundwater model - the groundwater flow process, *U.S. Geological Survey, Techniques and Methods*, 6-A16.
- Jäggli, C., J. Straubhaar, and P. Renard (2017), Posterior population expansion for solving inverse problems, *Water Resources Research*, *53*, 2902–2916, <http://dx.doi.org/10.1002/2016WR019550>.
- Jetchev, N., U. Bergmann, and R. Vollgraf (2016), Texture synthesis with spatial generative adversarial networks, *arXiv:1611.08207v2, [cs.CV]*, 1 Dec 2016.
- Kingma, D. P., and J. L. Ba (2015), ADAM: a method for stochastic optimization, *The International Conference on Learning Representations (ICLR)*, San Diego.
- Journel, A., and T. Zhang (2006), The necessity of a multiple-point prior model, *Mathematical Geology*, *38*(5), 591–610.
- Laloy, E., and J. A. Vrugt (2012), High-dimensional posterior exploration of hydrologic models using multiple-try DREAM_(ZS) and high-performance computing, *Water Resources Research*, *48*(1). <http://dx.doi.org/10.1029/2011WR010608>.
- Laloy, E., N. Linde, and J. A. Vrugt (2012), Mass conservative three-dimensional water tracer distribution from Markov chain Monte Carlo inversion of time-lapse ground-penetrating radar data, *Water Resources Research* *48*, W07510. <http://dx.doi.org/10.1029/2011WR011238>.
- Laloy, E., B. Rogiers, J. A. Vrugt, D. Mallants, and D. Jacques (2013), Efficient posterior exploration of a high-dimensional groundwater model from two-stage Markov Chain Monte Carlo simulation and polynomial chaos expansion, *Water Resources Research*, *49*, 2664–2682. <http://dx.doi.org/10.1002/wrcr.20226>.
- Laloy, E., N. Linde, D. Jacques, and J. A. Vrugt (2015), Probabilistic inference of multi-Gaussian fields from indirect hydrological data using circulant embedding and dimensionality reduction, *Water Resources Research*, *51*. <http://dx.doi.org/10.1002/2014WR016395>.
- Laloy, E., N. Linde, D. Jacques, and G. Mariethoz G (2016), Merging parallel tempering with sequential geostatistical resampling for improved posterior exploration of high-dimensional subsurface categorical fields, *Advances in Water Resources*, *90*, 57–69. <http://dx.doi.org/10.1016/j.advwatres.2016.02.008>.
- Laloy, E., R. Hérault, J. Lee, D. Jacques, and N. Linde (2017), Inversion using a new low-dimensional representation of complex binary geological media based on a deep neural network, *Under Review*.
- Lemmens, L., B. Rogiers, M. De Craen, E. Laloy, D. Jacques, M. Huysmans, R. Swennen, J. L. Urai, and G. Desbois (2017), Effective structural descriptors for natural and engineered radioactive waste confinement barrier, *EGU 2017 - poster 14094*.

- Li, X., G. Mariethoz, D.T. Lu, and N. Linde (2016), Patch-based iterative conditional geostatistical simulation using graph cuts, *Water Resources Research*, 52, 6297–6320, doi:10.1002/2015WR018378.
- Liang, X., Z. Hu, H. Zhang, C. Gan, and E. P. King (2017), Recurrent topic-transition GAN for visual paragraph generation, *arXiv:1703.07022v2, [cs.CV]*, 23 March 2017.
- Linde, N., and J. A. Vrugt (2013), Distributed soil moisture from crosshole ground-penetrating radar travel times using stochastic inversion, *Vadose Zone Journal*, 12(1). <http://dx.doi.org/doi:10.2136/vzj2012.0101>.
- Linde, N., P. Renard, T. Mukerji, and J. Caers, (2015), Geological realism in hydrogeological and geophysical inverse modeling: a review, *Advances in Water Resources*, 86, 86–101. <http://dx.doi.org/doi:10.1016/j.advwatres.2015.09.019>.
- Lochbühler, T., J. A. Vrugt, M. Sadegh, and N. Linde (2015), Summary statistics from training images as prior information in probabilistic inversion, *Geophysical Journal International*, 201, 157–171. <http://dx.doi:10.1093/gji/ggv008>.
- Lu, B., and S. Torquato (1992), Lineal-path function for random heterogeneous materials, *Physical Review, A* 45(2), 922.
- Mariethoz, G., P. Renard, and J. Straubhaar (2010), The Direct Sampling method to perform multiple-point geostatistical simulations, *Water Resources Research*, 46, W11536. <http://dx.doi.org/10.1029/2008WR007621>.
- Mariethoz, G., and J. Caers (2014), *Multiple-point geostatistics: stochastic modeling with training images*, Wiley.
- Mosser, L., O. Dubrule, and M. J. Blunt (2017), Reconstruction of three-dimensional porous media using generative adversarial neural networks, *arXiv:1704.03225v1, [cs.CV]*, 11 Apr 2017.
- Pardo-Igúzquiza, E., and P. Dowd (2003), CONNEC3D: A computer program for connectivity analysis of 3D random set models, *Computers and Geosciences*, 29, 775–785.
- Pirot, G., J. Straubhaar, and P. Renard (2015), A pseudo genetic model of coarse braided river deposits, *Water Resources Research*, 51(12), 9595–9611.
- Radford, A., L. Metz, and S. Chintala (2016), Unsupervised representation learning with deep convolutional generative adversarial networks (DCGANs), *The International Conference on Learning Representations (ICLR)*, San Juan, Puerto Rico.
- Robert, C.P., and G. Casella (2004), *Monte Carlo statistical methods*, second edition. Springer.
- Salimans, T., I. Goodfellow, W. Zaremba, V. Cheung, A. Radford, and X. Chen (2016), Improved techniques for training GANs, *arXiv:1606.03498, [cs.LG]*, 10 June 2016.
- Sønderby, S. K. , J. Caballero, L. Theis, W. Shi, and F. Huszár (2016), Amortised map inference for image super resolution, *arXiv:1610.04490v3, [cs.CV]*, 21 Feb 2017.
- Strebel, S. (2002), Conditional simulation of complex geological structures using multiple point statistics, *Mathematical Geology*, 34(1), 1–22.

- Tahmasebi, P., and M. Sahimi (2016), Enhancing multiple-point geostatistical modeling: 1. Graph theory and pattern adjustment, *Water Resources Research*, 52, 2074–2098, doi:10.1002/2015WR017806.
- Theano Development Team (2016), THEANO: A Python framework for fast computation of mathematical expressions, <http://arxiv.org/abs/1605.02688>.
- Torquato, S., and G. Stell (1982), Microstructure of two-phase random media. I. The n-point probability functions, *The Journal of Chemical Physics*, 77(4), 2071–2077.
- Torquato, S., J. D. Beasley, and Y. C. Chiew (1988), Two-point cluster function for continuum percolation, *The Journal of chemical physics*, 88(10), 6540–6547.
- Vo, H. X., and L. J. Durlofsky (2014), A new differentiable parameterization based on Principal Component Analysis for the low-dimensional representation of complex geological models, *Mathematical Geosciences*, 775–813.
- Vrugt, J. A., C. ter Braak, C. Diks, B. A. Robinson, J. M. Hyman, and D. Higdon (2009), Accelerating Markov chain Monte Carlo simulation by differential evolution with self-adaptive randomized subspace sampling, *International Journal of Nonlinear Sciences and Numerical Simulation*, 10(3), 273–290.
- Yang, L. C., S. Y. Chou, H., and Y. H. Yang (2017), MidiNet: a convolutional generative adversarial network for symbolic-domain music generation using 1D and 2D conditions, *arXiv:1703.10847v1, [cs.LG]*, 31 Mar 2017.
- Zahner, T., T. Lochbühler, G. Mariethoz, and N. Linde (2016), Image synthesis with graph cuts: a fast model proposal mechanism in probabilistic inversion, *Geophysical Journal International*, 204(2), 1179–1190. <http://dx.doi.org/10.1093/gji/ggv517>.